ADAPTIVE OPTICS ON LARGE TELESCOPES

A. GLINDEMANN[1*], S. HIPPLER[2], T. BERKEFELD[2] and W. HACKENBERG[3]

[1] *European Southern Observatory, Garching, Germany*
[2] *Max-Planck-Institut für Astronomie, Heidelberg, Germany*
[3] *Max-Planck-Institut für Extraterrestrische Physik, Garching, Germany*
* *author for correspondence, e-mail: aglindem@eso.org*

Abstract. Observations with ground based telescopes suffer from atmospheric turbulence. Independent of the telescope size the angular resolution in the visible is equivalent to that of a telescope with a diameter of 10–20 cm. This effect is caused by the turbulent mixing of air with different temperatures in the atmosphere. Thus, the perfect plane wave from a star at infinity is aberrated before it enters the telescope. In the following, we will discuss the physical background of imaging through turbulence, using Kolmogorov statistics, and the different techniques to sense and to correct the wave-front aberrations with adaptive optics. The requirements for the control loop of an adaptive optics system are discussed including formulas for the limiting magnitude of the guide star as a function of the wave-front sensing method, of the quality of the wave-front sensor camera, and of the degree of correction. Finally, a short introduction to deformable mirror technology will be given followed by the presentation of a new method to measure and to distinguish individual turbulent layers in order to increase the isoplanatic angle.

Keywords: adaptive optics, laser guide star

1. Introduction

The image quality of ground based telescopes suffers from atmospheric turbulence. Independent of the telescope size the angular resolution in the visible is equivalent to that of a telescope with a diameter of 10–20 cm. This effect is caused by the turbulent mixing of air with different temperatures in the atmosphere. Thus, the perfectly plane wave from a star at infinity is aberrated before it enters the telescope.

It was the idea of H. Babcock (1953) to correct these aberrations with a deformable mirror to obtain diffraction limited images. The principle of an adaptive optics system is displayed in Figure 1. The deformable mirror, a wave-front sensor and a camera in the corrected focus form the main elements. The wave-front sensor measures the aberrations with a high sampling rate and sends the control signals to the deformable mirror in order to correct the aberrations. Then, the corrected focus can be recorded by a camera with an exposure time independent of atmospheric turbulence.
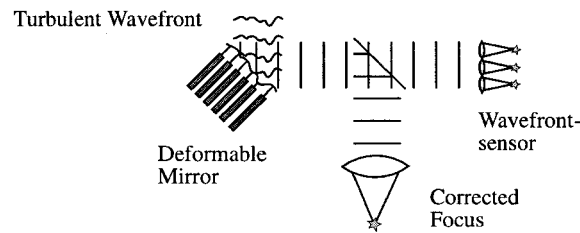
Figure 1. The main elements of an adaptive optics system. The wave-front sensor measures the aberrations and sends the information to the deformable mirror to flatten the wave-front. A camera in the corrected focus takes the corrected image.

Although this sounds simple, some demanding technical requirements for the wave-front sensor and for the deformable mirror delayed the realisation of adaptive optics systems by several decades. In the U.S. Air Force, adaptive optics systems were developed since 1970 in classified research (Hardy et al., 1977) both for improved imaging of satellites and for the projection of high energy laser beams onto missiles. In the civilian sector, it took until the late 1980's before the COME-ON system of the European Southern Observatory was installed on the 3.6-m telescope in Chile (Merkle et al., 1989). In the northern hemisphere, the PUEO adaptive optics system of the Canada-France-Hawaii Telescope was the first to become available to the astronomical community for regular science observations in 1996 (Rigaut et al., 1997).

The technical requirements for adaptive optics systems concern the sampling rate and the sensitivity of the wave-front sensor camera, and the frequency that can be applied to the deformable mirror. The required sampling rate is determined by the rate of changes of the atmospheric turbulences. Therefore, the statistical parameters of the turbulence play a vital role for adaptive optics systems. Kolmogorov statistics provide a suitable theoretical model for atmospheric turbulence. Measurements of the statistical properties have mostly confirmed the assumptions of this theory.

The most important question for the applicability of adaptive optics systems to astronomical research is the question about the sky coverage: how much of the sky can be observed given that a star of suitable brightness, the guide star in the wave-front sensor, has to be close to the object star? The required brightness of the guide star follows from the required sampling rate of the wave-front sensor camera determined by the rate of changes in the atmosphere, and from the desired degree of correction. In Figure 2, simulated short exposure images of a single star on a 3.5-m telescope under identical atmospheric conditions are displayed at different wavelengths. At 10 μm, a single diffraction limited speckle is moving around slowly, and image stabilisation is sufficient to create a diffraction limited image. In the visible at 0.5 μm, a speckle cloud of a few hundred speckles displays a dynamic behaviour similar to Brownian motion. Creating a single diffraction limited point spread function requires a deformable mirror with approximately as
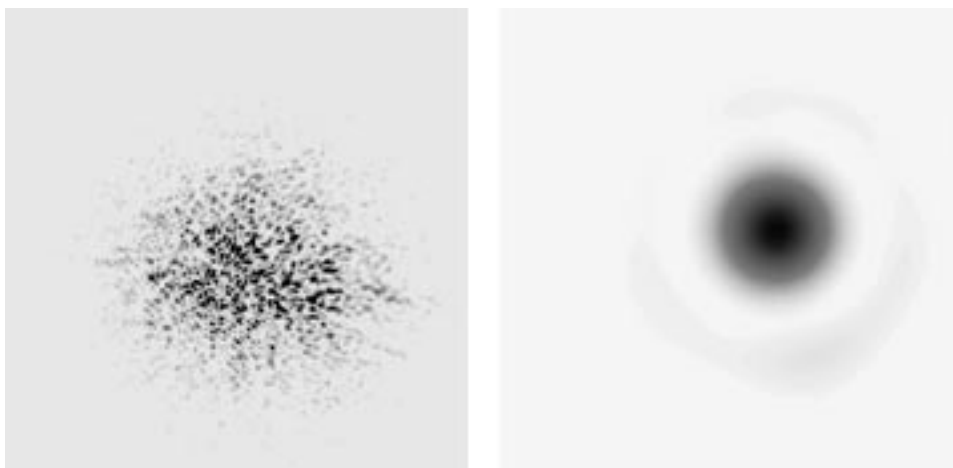
Figure 2. Speckle images of a single star in the visible at 0.5 μm (on the left) and at 10 μm (on the right) under identical atmospheric conditions on a 3.5-m telescope. In the 10 μm image, parts of the first diffraction ring can be seen. A simulation for atmospheric turbulence was used to produce the images.

many actuators as there are speckles. This example illustrates the very different requirements for the adaptive optics system at different wavelengths. Thus, the answer to the question about the sky coverage depends on the desired degree of correction and the subsequent parameters for wave-front sensor sampling rate, and on atmospheric conditions.

In the following, we will discuss the physical background of imaging through turbulence, and the different techniques to sense and to correct the aberrations caused by the turbulence. Examples of adaptive optics systems will demonstrate how the image improvement is done in practice.

The paper is organised as follows. In Section 2, after a short introduction to the notation used in Fourier optics, the Kolomogorov statistics and the impact on the imaging process are investigated. The components of adaptive optics systems are presented in Section 3 discussing methods for wave-front sensing and reconstruction, and the closed loop operation. The limiting magnitude of the guide star is expressed quantitatively as a function of the wave-front sensing method, of the quality of the wave-front sensor camera, and of the degree of correction.

Also in Section 3, the deformable mirror technology is introduced. A new method is discussed in Section 4 to measure and distinguish individual turbulent layers in order to increase the isoplanatic angle.

For further reading on this subject, the books by Tyson (1998) and by F. Roddier (ed., 1999) cover the field in great detail. Roggemann and Welsh (1996) devote several chapters in their book on imaging through turbulence to adaptive optics, and Beckers (1993) presents an overview of the applications of adaptive optics to astronomy. The conference proceedings of a NATO summer school on adaptive op-

tics, edited by D. Alloin and J.-M. Mariotti (1994), contain interesting contributions for the expert reader.

2.   Imaging through atmospheric turbulence

In the following, the relevant theoretical framework for understanding imaging through atmospheric turbulence will be discussed. For a more detailed description the reader is referred to the review by Roddier (1981) which is mainly based on the analysis of wave propagation in a turbulent medium by Tatarski (1961). The quantities and the underlying theory of the imaging process are briefly presented at the beginning of this section. Then, Kolmogorov's mathematical model to describe atmospheric turbulence is introduced (Kolmogorov, 1961), the statistical properties of the electromagnetic wave are discussed, and the impact on image motion and the appearance of the image are investigated.

2.1. PRELIMINARIES

The wave propagation through the atmosphere and the telescope into the focal plane is very conveniently described by Fresnel diffraction. Incorporating optical elements like lenses or mirrors in a spherical approximation leads to the well known Fourier relationship between the amplitude of the electromagnetic wave in the pupil of the telescope and the amplitude in its focal plane (Goodman, 1968; Born and Wolf, 1970; Marathay, 1982).

We use the notation $\Psi(\vec{x})$ for the complex amplitude in the telescope pupil and $A(\vec{u})$ for the complex amplitude in the focal plane. The two quantities are connected through a Fourier transform

$$A(\vec{u}) = \int \Psi(\vec{x}) \exp(2\pi i \vec{x}\vec{u}) \, d\vec{x},$$

where the integration is performed over the telescope pupil. The phase $\phi(\vec{x})$ of $\Psi(\vec{x})$ incorporates the turbulent atmosphere as well as the telescope aberrations. In the telescope focus, we are usually interested in the intensity distribution $I(\vec{u}) = |A(\vec{u})|^2$ that can be written as

$$\begin{aligned} I(\vec{u}) &= \iint \Psi(\vec{x}')\Psi^*(\vec{x}'') \exp(2\pi i (\vec{x}' - \vec{x}'')\vec{u}) \, d\vec{x}' d\vec{x}'' \\ &= \int \left(\int \Psi(\vec{x}')\Psi^*(\vec{x}' - \vec{x}) d\vec{x}' \right) \exp(2\pi i \vec{x}\vec{u}) \, d\vec{x}, \end{aligned}$$

where $\int \Psi(\vec{x}')\Psi^*(\vec{x}' - \vec{x}) d\vec{x}'$ is the autocorrelation of the amplitude in the telescope pupil that is called the optical transfer function (OTF). If a plane wave from a point

source at infinity enters a perfect, i.e. aberration free, telescope the OTF is a purely real function – approximately shaped like a triangle – and its Fourier transform is the diffraction limited point spread function, the Airy disk.

In the case of statistical fluctuations of the electromagnetic wave, due to an incoherent source or due to atmospheric turbulence, the autocorrelation can be expressed as an ensemble average over all possible realisations, called the coherence function:

$$\Gamma(\vec{x}) = <\Psi(\vec{x'})\Psi^*(\vec{x'} - \vec{x})> .$$

It is one of the main tasks of turbulence theory to connect the atmospheric properties to the coherence function in the telescope pupil and, thus, to its Fourier transform, the point spread function (PSF) in the telescope focal plane. If atmospheric turbulence rather than the telescope diameter limits the size of the PSF it is called the seeing disk and its full width at half maximum (FWHM) is called the *seeing*.

2.2. KOLMOGOROV TURBULENCE

The statistics of the spatial and temporal structure of atmospheric turbulence is of great importance to describing the propagation of light through the atmosphere. Following from the theory of fluid motion the flow of air becomes turbulent, i.e. unstable and random, if the *Reynolds number* $Re = L_0 v_0 / k_v$ exceeds a critical value, where L_0 is the characteristic size of the flow, v_0 is the characteristic velocity and k_v is the kinematic viscosity. With typical numbers for these parameters, $L_0 \approx 15$ m, $v_0 \approx 10$ m s^{-1} and $k_v = 15 \times 10^{-6}$ it is $Re \approx 10^5$ which corresponds to fully developed turbulence.

Kolmogorov (1961) suggested that the kinetic energy in the largest structures of the turbulence is transferred successively to smaller and smaller structures. He also assumed that the motion of the turbulent structure is both homogeneous and isotropic implying that the second and higher order statistical moments of the turbulence depend only on the distance between any two points in the structure. If the product of the characteristic size L of the small structure and its velocity v is too small to keep the Reynolds number in the turbulent regime the break up process stops and the kinetic energy is dissipated as heat by viscous friction. In a stationary state, the energy flow from larger structures L to smaller structures l must be constant, i.e. the amount of energy that is being injected into the largest structure must be equal to the energy that is dissipated as heat. It is $E(l)dl$ the kinetic energy of a structure with a size between l and $l + dl$. If the typical transfer time of $E(l)dl$ through a structure of size l is given by l/v the energy flow rate, ϵ_0, can be written as

$$\epsilon_0 = \frac{E(L)dL}{t(L)} = \frac{E(l)dl}{t(l)} = \frac{\frac{1}{2}\rho v^2}{l/v} = \text{const}, \tag{1}$$

and it is

$$v \propto l^{1/3}. \tag{2}$$

The kinetic energy $E(k)dk$ in the spectral range k and $k + dk$ is proportional to v^2. With the spatial frequency $k \propto l^{-1}$ one obtains

$$E(l)dl = E(k)dk \propto k^{-2/3} \text{ or } E(k) \propto k^{-5/3}. \tag{3}$$

For isotropic turbulence the three dimensional case can be calculated by integrating over the unit sphere:

$$E(k) = 4\pi k^2 E(\vec{k}) \Rightarrow E(\vec{k}) \propto k^{-11/3}. \tag{4}$$

This relationship expresses the Kolmogorov spectrum. It holds in the *inertial range* of turbulence for $L_0^{-1} \ll k \ll l_0^{-1}$ where L_0 is the outer scale of turbulence, generally the size of the largest structure that moves with homogeneous speed, and l_0 is the inner scale at which the viscous dissipation starts. The outer scale of turbulence varies between a few meters close to the ground where the largest structure is determined by the height over the ground, and a few hundred meters in the free atmosphere which is the thickness of the turbulent layer (Colavita, 1990; Tatarski and Zavoroty, 1993; Haniff et al., 1994). The inner scale of turbulence is in the range of a few millimetres near the ground to about 1 cm near the tropopause (Roddier, 1981).

2.3. INDEX-OF-REFRACTION FLUCTUATIONS

Light traveling through the atmosphere is affected by fluctuations of the refraction index. The physical source of these fluctuations are temperature inhomogeneities produced by turbulent mixing of air. The index of refraction as a function of wavelength is given by the Cauchy formula (Weast and Astle, 1981)

$$n(\lambda) = 1 + (272.6 + \frac{1.22}{\lambda^2})10^{-6}, \tag{5}$$

with λ in μm and the numerical parameters for 15 °C and 1000 mbar. $n(\lambda)$ for different temperatures is displayed in Figure 3. Both numerical parameters depend slightly on temperature and pressure. However, this dependence can be neglected in the second parameter (that is 1.22 in Equation 5), and the index of refraction $n(\vec{r})$ can be modelled as the sum of a purely wavelength dependent part $n(\lambda)$, and a randomly fluctuating part $n_f(\vec{r})$ depending on temperature and pressure. This approximation has the consequence that the shape of the wave-front is independent of the wavelength. Effects that show a wavelength dependence, like the different number of speckles in the optical and in the infrared, are caused by the different relative impact of the same wave-front distortion at different wavelengths.
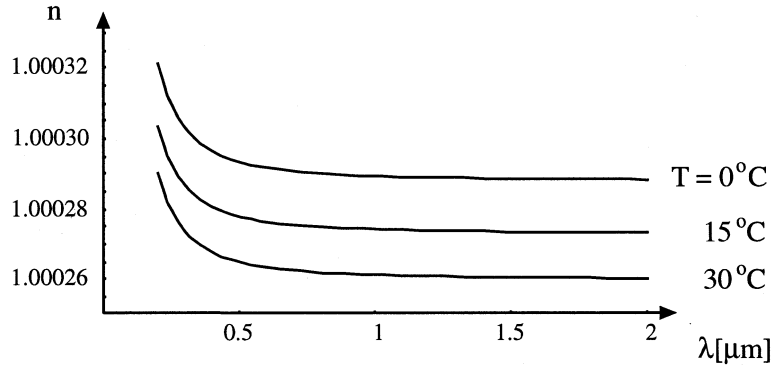
Figure 3. The refraction index of air at 0, 15 and 30 °C and 1000 mbar as given by the Cauchy formula. The dependence on temperature can be modeled by approximating the refraction as a sum of temperature and wavelength dependent terms.

Using $n(\lambda) \approx 1$, the refraction index as a function of temperature and pressure at optical and near infrared wavelengths can be written as (Ishimura, 1978)

$$n(\vec{r}) - 1 = n_f(\vec{r}) = \frac{77.6\,P}{T} 10^{-6}, \tag{6}$$

where T is the temperature of the air in Kelvin and P the pressure in millibar. It can be shown that the refraction index as a passive, conservative additive, i.e. a quantity that does not affect atmospheric turbulences and that is not affected by the motion of the air, also follows Kolmogorov statistics (Obukhov, 1949). Then, the power spectral density $\Phi_n(k)$ of $n(\vec{r})$ has the same spatial frequency dependence as the kinetic energy and can be expressed as

$$\Phi_n(k) = 0.033\,C_n^2\,k^{-11/3}. \tag{7}$$

The quantity C_n^2 is called the *structure constant* of the refraction index fluctuations and has units of m$^{-2/3}$. It characterises the strength of the refraction index fluctuations. Measurements of C_n^2 have shown a good agreement with the Kolmogorov theory (see e.g. Hufnagel, 1974; Clifford, 1978). The latest measurements of C_n^2 have been performed by Klückers et al. (1997) using a method suggested by Vernin and Roddier (1973).

Based on measurements Hufnagel and Valley (1980) suggested a model for the atmospheric turbulence profile called the Hufnagel-Valley-Boundary model. Since the profile varies from site to site and from time to time this model can only give a rough idea of the layer structure. The structure constant can be modelled using the formula

$$C_n^2(h) = 2.2 \times 10^{-23}h^{10}e^{-h} + 10^{-16}e^{-h/1.5} + 1.7 \times 10^{-14}e^{-h/0.1}. \tag{8}$$

Like the statistical distribution of velocity discussed in Section 2.2 the refraction index distribution is isotropic and homogeneous as long as the spatial frequencies

involved are in the inertial range, with $L_0^{-1} \ll k \ll l_0^{-1}$. The Kolmogorov theory predicts a mathematical form for $\Phi_n(k)$ only inside the inertial range. The von Karman spectrum (Ishimura, 1978) models the power spectral density also outside of this regime.
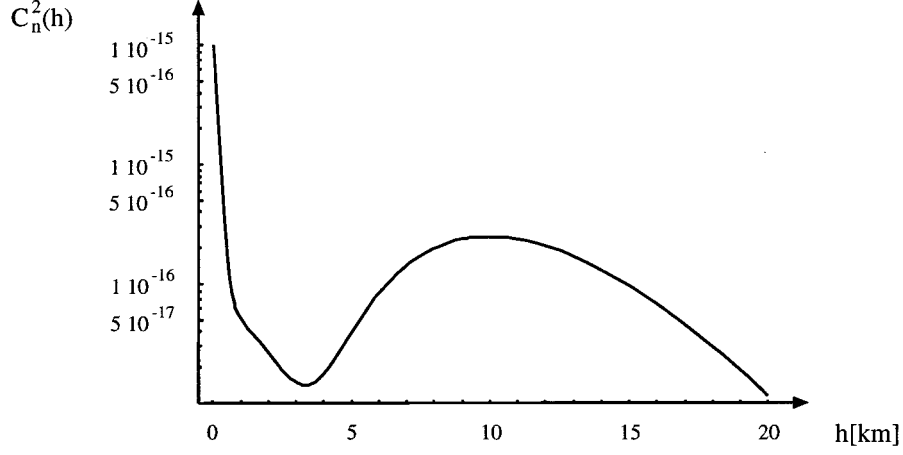

Figure 4. Average C_n^2 profile as a function of altitude in km as given by the Hufnagel-Valley-Boundary model. Two distinct layers can be distinguished, near the ground (100 m) and at 10 km.

So far, only the power spectral density of the refraction index fluctuations has been discussed. The power spectral density is related to the autocorrelation $\Gamma_n(\vec{r}) = < n(\vec{r_1})n(\vec{r_1} + \vec{r}) >$ by the Wiener-Khinchin theorem:

$$\Gamma_n(\vec{r}) = \int \Phi_n(|\vec{k}|)e^{-2\pi i \vec{k}\vec{r}}d\vec{k}. \tag{9}$$

As already noted, the random process leading to the fluctuation of the refractive index is isotropic and homogeneous. Thus, second and higher moments of n, like the autocorrelation depend only on the distance between two points. This allows us to express both the power spectral density and the autocorrelation as functions of the three dimensional vectors $\vec{k}$ and $\vec{r}$ where $|\vec{k}|$ and $|\vec{r}|$ are denoted by k and r respectively. To avoid the integration over the pole at $k = 0$ the *structure function* of the refraction index is introduced as

$$\begin{aligned} D_n(r) &= < |n(r_1) - n(r_1 + r)|^2 > \\ &= 2(< n(r_1)^2 > - < n(r_1)n(r_1 + r) >) \\ &= 2(\Gamma_n(0) - \Gamma_n(r)) \,. \end{aligned}$$

The result of this calculation was derived by Obukhov (1949):

$$D_n(r) = C_n^2 r^{2/3}. \tag{10}$$

This form of the structure function of the refractive index is known as Obukhov's law. Together with the Kolmogorov spectrum (Equation 7) it forms the basis for the description of wave propagation through turbulence.

2.4. STATISTICAL PROPERTIES OF THE ABERRATED COMPLEX WAVE

For the sake of simplicity, only horizontal monochromatic plane waves are considered, propagating downwards through atmospheric turbulence from a star at zenith. The fluctuations of the complex amplitude are calculated by using the Kolmogorov spectrum and Obukhov's law.

Using the thin screen approximation (Roddier, 1981), the layer thickness is assumed to be large compared to the correlation scale of the fluctuations but small enough to neglect diffraction effects within the layer. Also, the layer is non-absorbing and its statistical properties depend only on the altitude h, i.e. the structure constant C_n^2 does not vary in the horizontal direction. After propagation through a thin turbulent layer at altitude h, the phase is related to the distribution of the refractive index through

$$\phi_h(\vec{x}) = \frac{2\pi}{\lambda} \int_h^{h+\delta h} n(\vec{x}, z) dz, \tag{11}$$

where δh is the thickness of the layer and $\vec{x} = (x, y)$ denotes the horizontal coordinate vector. The complex amplitude after propagation through a layer at altitude h can be written as

$$\Psi_h(\vec{x}) = e^{i\phi_h(\vec{x})}. \tag{12}$$

To describe the statistical properties of the complex wave we need the correlation function of the complex amplitude, the coherence function, defined as

$$\begin{aligned} \Gamma_h(\vec{x}) &= <\Psi_h(\vec{x'})\Psi_h^*(\vec{x'} + \vec{x})> \\ &= <e^{i[\phi_h(\vec{x'})-\phi_h(\vec{x'}+\vec{x})]}> . \end{aligned} \tag{13}$$

As the intensity distribution in the telescope focal plane is the Fourier transform of the coherence function in the telescope aperture, its description as a function of the atmospheric properties determines the telescope point spread function affected by atmospheric turbulence, i.e. the seeing disk. Since the phase $\phi_h(\vec{x})$ is the sum of a large number of independent variables (the refraction indices $n(\vec{x}, z)$, Equation 11) it is reasonable to apply the central-limit theorem implying that $\phi_h(\vec{x})$ and also $\phi_h(\vec{x'}) - \phi_h(\vec{x'} + \vec{x})$ follow Gaussian statistics. Then, the expectation value in Equation (13) is called the characteristic function of the Gaussian random process, and it is defined as

$$<e^{izv}> = \int e^{izx} p_v(x) dx = e^{-\frac{1}{2}<v^2>z^2}, \tag{14}$$

where $p_v(x)$ denotes the Gaussian distribution of the random variable v. In Equation (13) v is the Gaussian distributed phase difference $\phi_h(\vec{x'}) - \phi_h(\vec{x'} + \vec{x})$ and z equals unity. Using these properties, the coherence function can be written as

$$\Gamma_h(\vec{x}) = e^{-\frac{1}{2} < [\phi_h(\vec{x'}) - \phi_h(\vec{x'} + \vec{x})]^2 >}, \tag{15}$$

or, introducing the phase structure function $D_{\phi,h}(\vec{x}) = < [\phi_h(\vec{x'}) - \phi_h(\vec{x'} + \vec{x})]^2 >$,

$$\Gamma_h(\vec{x}) = e^{-\frac{1}{2} D_{\phi,h}(\vec{x})}. \tag{16}$$

The problem of determining the coherence function of the complex amplitude is now shifted to calculating the phase structure function $D_{\phi,h}(\vec{x})$. The relation between the three-dimensional distribution of the refraction index and the two-dimensional distribution of the phase is given by Equation (11). This leads from the three-dimensional structure function of the refraction index (Equation 10) to the one of the phase $D_{\phi,h}(\vec{x})$ that depends on the two-dimensional vector $\vec{x}$. Assuming also that δh is much larger than the correlation scale of the fluctuations, one can show that for a horizontal wave-front entering the layer i at altitude h_i, the phase structure function at the exit of the layer is (Fried, 1966)

$$D_{\phi,h_i}(x) = 2.91(\frac{2\pi}{\lambda})^2 \delta h_i C_{n_i}^2 x^{5/3}, \tag{17}$$

with $x = |\vec{x}|$.

Calculating the coherence function iteratively for multiple layers one obtains the coherence function on the ground in the telescope aperture after propagation through N turbulent layers as

$$< \Psi_0(x') \Psi_0^*(x' + x) > \, = e^{-\frac{1}{2} D_{\phi,0}(x)}, \text{ with}$$

$$D_{\phi,0}(x) = 2.91(\frac{2\pi}{\lambda})^2 \sum_{i=1}^{N} \delta h_i C_{n_i}^2 \, x^{5/3}. \tag{18}$$

The distances between the layers and the size of the diffraction structures are such that the propagation of the complex amplitude has to be described by Fresnel diffraction. That means that the complex amplitude on the ground fluctuates both in amplitude and in phase. The propagation of the coherence function through the atmosphere, however, is reduced to a simple product of the coherence functions of the single layers, unaffected by Fresnel diffraction (Roddier, 1981). This reflects the general property of the coherence function that Fresnel terms cancel when describing the propagation of the coherence function through space or through an optical system (Marathay, 1982).

In the case of a continuous distribution of turbulence and of a source at zenith distance γ one obtains

$$D_{\phi,0}(x) = 2.91 (\frac{2\pi}{\lambda})^2 (\cos \gamma)^{-1} x^{5/3} \int C_n^2(h)dh. \tag{19}$$

$D_{\phi,0}$ is the phase structure function of the phase in rad. If the phase is given in the dimension of meter it describes the physical shape of the turbulent wave-front. It is interesting to note that the phase structure function of the phase in meter, and thus the shape of the phase, is independent of wavelength. This follows from the approximation $n(\vec{r}) = n(\lambda) + n_f(\vec{r})$. Therefore, a wave-front sensor can be operated in the visible determining the shape of the wave-front and steering the deformable mirror for observations in the infrared.

Fried further simplified the expression by introducing the quantity r_0, called the Fried parameter (Fried, 1965a), which is defined by

$$r_0 = \left(0.423 \ (\frac{2\pi}{\lambda})^2 (\cos \gamma)^{-1} \int C_n^2(h)dh \right)^{-3/5}. \tag{20}$$

The wavelength dependence of r_0 is given by $r_0 \propto \lambda^{6/5}$ and the dependence on zenith angle is $r_0 \propto (\cos \gamma)^{3/5}$. The phase structure function in the telescope pupil can now be expressed by

$$D_{\phi,0}(x) = 6.88 \left(\frac{x}{r_0} \right)^{5/3}, \tag{21}$$

and the coherence function in the telescope pupil is

$$\Gamma_0(x) = < \Psi_0(x')\Psi_0^*(x' + x) > = e^{-3.44(\frac{x}{r_0})^{5/3}}. \tag{22}$$

If a single star is observed through the telescope the turbulence limited point spread function is obtained by computing the Fourier integral of the coherence function over the circular telescope aperture. Figure 5 displays the turbulence limited point spread function, that is called the seeing disk. A Gaussian function models the seeing disk reasonably well. However, with the Gaussian approximation the seeing disk converges to zero much faster than measured seeing profiles that are better described by the Kolmogorov model. The full width half maximum (FWHM) of the seeing disk is $0.98\lambda/r_0$ corresponding in good approximation to a telescope with diameter r_0. With $r_0 \propto \lambda^{6/5}$ the seeing is $\lambda/r_0 \propto \lambda^{-1/5}$, i.e. it is decreasing slowly with increasing wavelength.
Very often the power spectrum of the phase fluctuations is needed for analysis. Similar to the calculation that related the Kolmogorov spectrum of refractive index fluctuations (Equation 7) to the structure function of the refractive index (Equation 10)
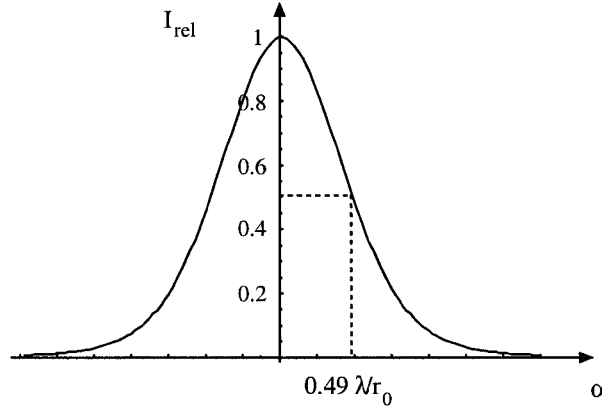
Figure 5. The intensity distribution in a seeing disk in arbitrary units calculated numerically using the phase structure function $D_\phi(x) = 6.88\left(\frac{x}{r_0}\right)^{5/3}$. The full width at half maximum (FWHM) is approximately λ/r_0.

the Kolmogorov power spectrum of the phase fluctuations can be calculated (Noll, 1976), yielding

$$\Phi(k) = 0.023\, r_0^{-5/3}\, k^{-11/3}. \tag{23}$$

The integral over the power spectrum gives the variance of the phase. As noted above, the integral over $\Phi(k) \propto k^{-11/3}$ is infinite. This means, that the variance of the turbulent phase is infinite which is a well known property of Kolmogorov turbulence. If the outer scale is finite the (now finite) variance can be calculated using the von Karman spectrum (Ishimura, 1978). In general, the phase variance increases with increasing outer scale.

2.5. ANISOPLANATIC AND TEMPORAL EFFECTS

So far we have discussed a single plane wave originating from a star at an angular distance γ from zenith. By calculating the coherence function as the ensemble average over many realisations of the atmospheric turbulence we have effectively determined the time average and, thus, the time averaged seeing disk. A snapshot image of a single random realisation of the turbulence displays the well known speckle image caused by the quasi frozen turbulence of the atmosphere. The light of a star at a slightly different angular position travels through slightly different portions of the atmosphere – the more different the higher the contributing layers are – and displays a different speckle pattern. However, the long time exposures of the two stars are identical as long as the statistical characteristics of the turbulent layers, i.e. C_n^2, do not differ. In speckle interferometry this property allows the use of a reference star that might be separated by several degrees from the science object but that still has the same statistical parameters.

In adaptive optics systems the guide star has to be very close to the observed object in order to measure a wave-front that closely resembles the object wave-front. The two quantities, the acceptable angular distance between the object and the guide star (the isoplanatic angle), and the rate of the temporal decorrelation of the turbulence that determines the required sampling rate of the wave-front sensor camera, are the most important limiting factors for the performance.

The isoplanacy can be quantified in a very simple way: The displacement by an angle $\vec{\theta}$ is replaced by the lateral shift $\vec{\theta}h$ of the relevant layer at altitude h, and the phase distribution in the observing direction $\vec{\theta} + \vec{\theta}'$ can be expressed by a shift of the phase at $\vec{\theta}'$:

$$\phi(\vec{x}, \vec{\theta} + \vec{\theta}') = \phi(\vec{x} - \vec{\theta}h, \vec{\theta}'). \tag{24}$$

The angular phase structure function, describing the correlation between the phase distribution in $\vec{\theta}$ and $\vec{\theta}'$ can be written as

$$
\begin{aligned}
D_\phi(\vec{\theta}) &= \; < [\phi(\vec{x}, \vec{\theta}') - \phi_h(\vec{x} - \vec{\theta}h, \vec{\theta}')]^2 > \\
&= \; 6.88 \left(\frac{\theta h}{r_0} \right)^{5/3}.
\end{aligned}
\tag{25}
$$

The influence of different layers with different wind speeds can be investigated by applying the individual altitudes h_i of the individual layers i with structure constants $C_{n_i}^2$ (see Equation 18) and performing the summation.

For the simplest case of a single dominant layer at altitude h an isoplanatic angle can be defined as $\theta_0 = r_0/h$. Thus, if the main turbulent layer is at an altitude of 10 km and $r_0 = 60$ cm, which corresponds to $0.76''$ seeing in the near infrared at $\lambda = 2.2\ \mu$m*, it is $\theta_0 = 12''$. This value can only give an idea of the order of magnitude of the isoplanatic angle. In practical cases the value depends on the particular composition of the atmosphere and the degree of the adaptive correction. For low order adaptive optics, e.g. a tip-tilt system or low altitude layers the angle may be much larger.

Using the Taylor hypothesis of frozen turbulence the temporal evolution can be estimated. The assumption is that a static layer of turbulence moves with constant speed $\vec{v}$ in front of the telescope aperture. Then the phase at point $\vec{x}$ at time $t' + t$ can be written as

$$\phi(\vec{x}, t' + t) = \phi(\vec{x} - \vec{v}t, t'), \tag{26}$$

and the temporal phase structure function is

$$D_\phi(\vec{v}t) = < [\phi(\vec{x}, t') - \phi(\vec{x} - \vec{v}t, t')]^2 > . \tag{27}$$

* The atmospheric window at $2.2\pm0.2\ \mu$m is called the K-band. Most of the numerical examples will be given for this band.

The temporal difference is thus transformed to a difference in spatial coordinates with the difference being $\vec{v}t$. The phase structure function depends individually on the two coordinates parallel and perpendicular to the wind direction. In the direction of the wind speed a simple estimate of the correlation time similar to the isoplanatic angle above yields the coherence time $\tau_0 = r_0/|\vec{v}|$. A wind speed of $v = 10$ m s^{-1} and a Fried parameter of $r_0 = 60$ cm give a coherence time of $\tau_0 = 60$ msec. In speckle interferometry, this is approximately the exposure time that can be used for single speckle images. For adaptive optics the reciprocal of the coherence time indicates the required bandwidth of the closed loop correction system. Greenwood and Fried (1976), after more elaborate analysis, gave a definition for the required bandwidth, the so-called Greenwood frequency that is often used to specify adaptive optics system. For a single turbulent layer this frequency is $f_G = 0.43v/r_0$ (see Section 3.3). Multiple layers with different speeds are considered equivalently to the case of anisoplanacy by applying individual speed vectors to individual layers with structure constants $C_{n_i}^2$ (Roddier et al., 1982).

The temporal power spectrum of the phase fluctuations can be calculated from the spatial power spectrum $\Phi(|\vec{k}|)$ (Equation 23). With $\vec{v}$ being e.g. parallel to the x axis, it is $k_x = f/v$ and an integration over k_y is performed to obtain the temporal power spectrum $\Phi_t(f)$ (Conan et al., 1995a),

$$\Phi_t(f) = 1/v \int \Phi(f/v, k_y) \, dk_y = 0.077 \, r_0^{-5/3} \, \frac{1}{v} \, \left(\frac{f}{v}\right)^{-8/3}. \tag{28}$$

The variance of the phase fluctuations is the integral over the temporal power spectrum. As there is a pole at $f = 0$ this integral is infinite which is the well known property of Kolmogorov turbulence discussed above (Tatarski, 1961). This integral can be computed if the outer scale L_0 is taken to be finite. As already noted, the Kolmogorov spectrum is not defined outside the inertial range and the von Karman spectrum has to be used to perform the integration.

2.6. IMAGE MOTION

In the last section, the statistical properties of the propagating turbulent wave-front have been described. When it comes to analysing the imaging process in the telescope, some assumptions have to be made about the phase distribution in the telescope aperture. We assume that the turbulent atmosphere can be represented by a single thin layer in the telescope aperture neglecting the effects of Fresnel diffraction, e.g. scintillation, discussed in Section 2.4 (Roddier, 1981).

The average gradient of the phase distribution in the telescope aperture determines the position of the image in the telescope focus. Although this is a low-order effect of atmospheric turbulence on the imaging process it is worthwhile discussing it in more detail as it determines the requirements for wave-front sensors like the Shack-Hartmann sensor that rely on reconstructing the wave-front from gradient measurements in the subapertures.

First we discuss the statistical properties of the gradient $\vec{\theta}$ of the wave-front without averaging over the telescope aperture. The two components θ_x and θ_y as a function of the horizontal coordinate $\vec{x} = (x, y)$ are (Roddier, 1981)

$$\theta_x(x, y) = -\frac{\lambda}{2\pi} \frac{\partial}{\partial x} \phi(x, y) \text{ and } \theta_y(x, y) = -\frac{\lambda}{2\pi} \frac{\partial}{\partial y} \phi(x, y) . \qquad (29)$$

The power spectra of the two vector components $\Phi_{\theta_x}(\vec{k})$ and $\Phi_{\theta_y}(\vec{k})$ are related to the power spectrum of the phase $\Phi(|\vec{k}|)$ by $\Phi_{\theta_{x,y}}(\vec{k}) = \lambda^2 k_{x,y}^2 \Phi(|\vec{k}|)$, yielding

$$\Phi_\theta(k) = 0.023\lambda^2 (k_x^2 + k_y^2) r_0^{-5/3} k^{-11/3} = 0.023\lambda^2 r_0^{-5/3} k^{-5/3}. \qquad (30)$$

The effect of averaging the gradient over the telescope aperture is considered by convolving the gradient in Equation (29) with the aperture function $A(\vec{x})$ that usually has a circular shape. The central obscuration usually can be neglected. The averaged gradient can be written as

$$\theta_x^D(\vec{x}) = \int \theta_x(\vec{x'}) A(\vec{x} - \vec{x'}) d\vec{x'}, \qquad (31)$$

where the superscript D indicates the average over the aperture D. For a point like aperture the averaging process collapses yielding $\theta_x^D(\vec{x}) = \theta_x(\vec{x'})$. The convolution transforms into a multiplication in Fourier space and one obtains the power spectrum of the phase gradient after averaging with the telescope aperture (Martin, 1987; Conan et al., 1995)

$$\Phi_\theta^D(k) = 0.023\lambda^2 r_0^{-5/3} k^{-5/3} \left| \frac{2J_1(\pi Dk)}{\pi Dk} \right|^2 , \qquad (32)$$

with J_1 the first order Bessel function describing the diffraction limited point spread function, the Airy disk, which is the Fourier transform of the circular aperture (Born and Wolf, 1970). The Bessel function acts as a low pass filter on the power spectrum. The contributions at high frequencies corresponding to small distances in the turbulent wave-front are reduced as the averaging process smoothes the gradients. At low frequencies, i.e. for large distances the effect of the pupil averaging is much reduced and the power spectrum is unaffected.

The variance of the image motion can be calculated by integrating over the power spectrum $\Phi_\theta^D(k)$ yielding the two-axis variance of the position θ of the image centroid as (Tyler, 1994)

$$(\Delta\theta)^2 = 0.34(\lambda/r_0)^2 (D/r_0)^{-1/3} [\text{arcsec}^2], \qquad (33)$$

with λ/r_0 the seeing in arcsec. The quotient D/r_0 will appear in all those formulas that describe the imaging process in the telescope. In practical cases it can be

calculated quite easily as it relates the size of the seeing disk λ/r_0 to the FWHM of the Airy pattern λ/D, $\frac{\lambda/r_0}{\lambda/D} = D/r_0$. In 0.76″ seeing at 2.2 μm on a 3.5-m telescope it is $D/r_0 = 6$.

The dependence of $(\Delta\theta)^2$ on $D^{-1/3}$ means that the variance of the image motion increases with decreasing telescope diameter. It is important to note that $(\Delta\theta)^2$ is independent of wavelength; the image motion in arcsec is the same at all wavelengths. Thus, wave-front sensors like the Shack-Hartmann sensor measuring the wave-front gradient can be operated in the visible for corrections at all wavelengths.

2.6.1. *Temporal evolution of image motion*

The Taylor hypothesis of frozen turbulence is used again to estimate the effect of moving turbulence. The temporal power spectrum of the averaged phase gradient can be calculated similar to the one of the phase (Equation 28) by integrating over the direction perpendicular to the wind speed. It is

$$\Phi_{\theta,t}(f) = 1/v \int \Phi_\theta^D(f/v, k_y) \, dk_y. \tag{34}$$

This integral cannot be solved in closed form. Tyler (1994) gave an approximation for the power spectrum at low and high frequencies that can be simplified by assuming that there is one dominant layer with wind speed $\hat{v}$ (Glindemann, 1997b). Then, the power spectral density of the centroid motion in the two regimes are

$$\begin{aligned}
P_{f_{\text{low}}} &= 0.096(r_0/\hat{v})^{1/3}(\lambda/r_0)^2 f^{-2/3}[\text{arcsec}^2/\text{Hz}], \\
P_{f_{\text{high}}} &= 0.0013(D/\hat{v})^{-8/3}(\lambda/r_0)^2 (D/r_0)^{-1/3} f^{-11/3}[\text{arcsec}^2/\text{Hz}],
\end{aligned} \tag{35}$$

where λ/r_0 is the seeing in arcsec. In Figure 6, $P_{f_{\text{low}}}$ and $P_{f_{\text{high}}}$ are displayed and compared to measured power spectra. In the low frequency region the power spectrum decreases with $f^{-2/3}$ and it is independent of the size of the aperture D. In the high frequency region the spectrum is proportional to $f^{-11/3}$ decreasing with D^{-3}. This illustrates the influence of the Bessel function as a low pass filter that leaves the low frequency region unaffected by the aperture and that takes effect as soon as the frequency is beyond a value of $f_t = 0.24\hat{v}/D$ which is the transient region between the two approximations. This value agrees well with the value given by Conan et al. (1995). Because of the steep slope ($\propto f^{-11/3}$) of the power spectrum at frequencies beyond the transient frequency f_t the contributions to the image motion are very small. Thus, a tip-tilt system that stabilises the image motion must have a bandwidth of approximately f_t to correct for most of the turbulence induced image motion. In Kasper et al. (2000), the bandwidth requirements will be discussed in greater detail.

The increasing variance of the image motion with smaller apertures D can now be attributed to an increase of the power spectrum in the high frequency region. In order to stabilise the image motion on smaller telescopes the correction frequency has to be higher. It is interesting to note that if the telescope aperture is larger than
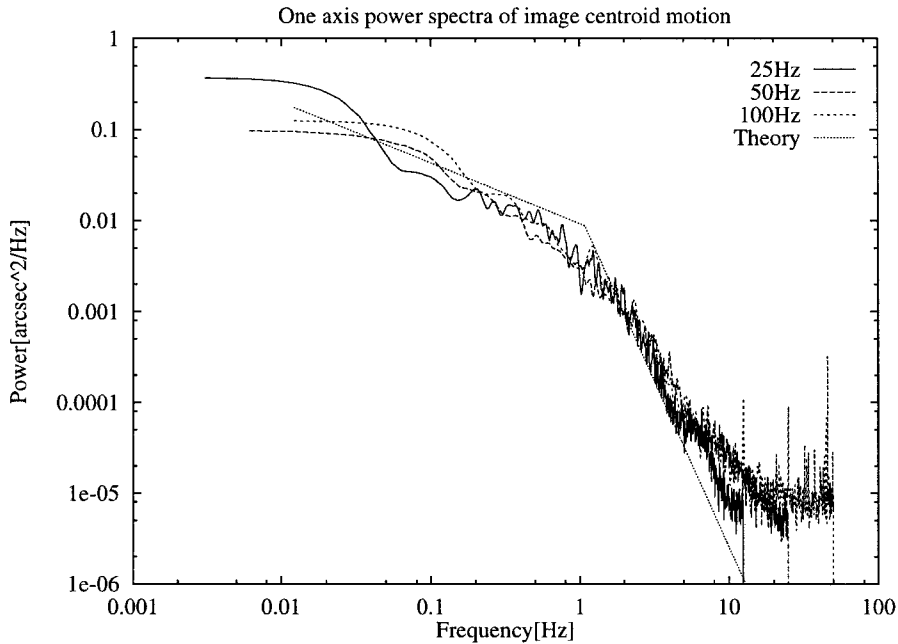
Figure 6. Measured power spectra of the image centroid motion on a 3.5-m telescope for different sampling frequencies. The dashed lines display the approximation for the same seeing and wind parameters. From the transient frequency of about $f_t = 1$ Hz and $D = 3.5$ m the effective wind speed can be estimated to be $\hat{v} \approx 14$ m s^{-1}. The measurements agree very well with each other and reasonably well with the theoretical curve (dotted line) (Glindemann, 1997b).

the outer scale of turbulence L_0 the image motion is reduced below the values predicted by Kolmogorov statistics. This affects in particular the fringe motion on telescope interferometers with a baseline longer than L_0.

2.7. ZERNIKE REPRESENTATION OF ATMOSPHERIC TURBULENCE

In the theory of optical aberrations Zernike polynomials are used very often to describe the aberrations. They were introduced in 1934 by F. Zernike who deduced them from the Jacobi polynomials and slightly modified them for the application in optics (Zernike, 1934). Zernike polynomials have the advantage that they are mathematically well defined and that the low order terms are related to the classical aberrations like astigmatism, coma and spherical aberration.

Since the Zernike polynomials are defined on the unit circle and since we are interested in the turbulent wave-front in the circular telescope aperture it is useful to express the wave-front in terms of the Zernike polynomials. The influence of the central obscuration is negligible. Noll (1976) introduced a normalisation for the polynomials that is particularly suited for application to Kolmogorov turbulence. In this normalisation the rms value of each polynomial over the circle is set equal

TABLE I

Zernike polynomials Z_j for $j = 1$ to 11. n is the radial order and m the azimuthal order. The modes are ordered such that even j correspond to the symmetric modes given by $\cos m\theta$ and odd j to the antisymmetric modes given by $\sin m\theta$

n	$m = 0$	$m = 1$	$m = 2$	$m = 3$
0	$Z_1 = 1$ (piston)			
1		$Z_2 = 2\rho \cos\theta$ $Z_3 = 2\rho \sin\theta$ (tip and tilt)		
2	$Z_4 = \sqrt{3}\,(2\rho^2 - 1)$ (focus)		$Z_5 = \sqrt{6}\,\rho^2 \sin 2\theta$ $Z_6 = \sqrt{6}\,\rho^2 \cos 2\theta$ (astigmatism)	
3		$Z_7 = \sqrt{8}(3\rho^3 - 2\rho) \sin\theta$ $Z_8 = \sqrt{8}(3\rho^3 - 2\rho) \cos\theta$ (coma)		$Z_9 = \sqrt{8}\rho^3 \sin 3\theta$ $Z_{10} = \sqrt{8}\rho^3 \cos 3\theta$ (trifoil)

to one. The Zernike polynomials form a set of orthogonal polynomials and it is convenient to write them as a function of ρ and θ:

$$
\begin{aligned}
Z_{j_{\text{even}}} &= \sqrt{n+1}\, R_n^m(\rho)\sqrt{2}\,\cos(m\theta), \ \text{for } m \neq 0, \\
Z_{j_{\text{odd}}} &= \sqrt{n+1}\, R_n^m(\rho)\sqrt{2}\,\sin(m\theta), \ \text{for } m \neq 0, \\
Z_j &= \sqrt{n+1}\, R_n^0(\rho), \ \text{for } m = 0,
\end{aligned}
\tag{36}
$$

where

$$
R_n^m(\rho) = \sum_{s=0}^{\frac{n-m}{2}} \frac{(-1)^s (n-s)!}{s!(\frac{n+m}{2} - s)!\,(\frac{n-m}{2} - s)!}\, \rho^{n-2s}.
\tag{37}
$$

Table I shows the low order Zernike polynomials where the columns m indicate the azimuthal orders and the rows n the radial orders.

The polynomial expansion of the arbitrary wave-front $\phi(\rho, \theta)$ over the unit circle is defined as

$$
\phi(\rho, \theta) = \sum_{i=1}^{\infty} a_i Z_i(\rho, \theta),
\tag{38}
$$

TABLE II

The residual variance Δ_j of Kolmogorov turbulence after the first j Zernike modes are removed. The difference in the right column illustrates the strength of the single modes demonstrating that modes of equal radial order contribute the same amount to the variance

$\Delta_1 = 1.030(D/r_0)^{5/3}$	
$\Delta_2 = 0.582(D/r_0)^{5/3}$	$\Delta_2 - \Delta_1 = 0.448$
$\Delta_3 = 0.134(D/r_0)^{5/3}$	$\Delta_3 - \Delta_2 = 0.448$
$\Delta_4 = 0.111(D/r_0)^{5/3}$	$\Delta_4 - \Delta_3 = 0.023$
$\Delta_5 = 0.0880(D/r_0)^{5/3}$	$\Delta_5 - \Delta_4 = 0.023$
$\Delta_6 = 0.0648(D/r_0)^{5/3}$	$\Delta_6 - \Delta_5 = 0.023$
$\Delta_7 = 0.0587(D/r_0)^{5/3}$	$\Delta_7 - \Delta_6 = 0.0062$
$\Delta_8 = 0.0525(D/r_0)^{5/3}$	$\Delta_8 - \Delta_7 = 0.0062$

and the coefficients a_i, using the orthogonality, are given by

$$a_i = \int_{\text{aperture}} \phi(\rho, \theta) Z_i(\rho, \theta) \rho d\rho d\theta . \tag{39}$$

The convenience of the Zernike polynomials lies in the property that, following from the Kolmogorov statistics, one can determine individually the power in every single mode like tip-tilt, astigmatism or coma. One can then immediately calculate the residual aberration after correcting a specified number of modes with an adaptive optics system. This computation was done by Noll (1976). The variance of the residual aberration is expressed as the variance of the difference between the uncorrected phase and of the removed modes. If the aberration that is due to the first J Zernike polynomials is written as

$$\phi_J(\rho, \theta) = \sum_{i=1}^{J} a_i Z_i(\rho, \theta), \tag{40}$$

the variance of the remaining aberrations can be expressed as

$$\Delta_J = \iint_{\text{aperture}} < [\phi(\rho, \theta) - \phi_J(\rho, \theta)]^2 > \rho d\rho d\theta. \tag{41}$$

As already noted, the variance of the phase fluctuations $< \phi^2(\rho, \theta) >$ is infinite. The analysis in terms of Zernike polynomials shows that the infinity lies in the piston term. Removing the piston term gives a finite value for the variance of

the residual aberration. The residual variances in Table II are given in terms of $(D/r_0)^{5/3}$ as the Zernike polynomials are defined in the telescope aperture D. The right column of the table shows the differential improvement. It shows that the differences are constant for the same radial degree n. For the removal of higher orders Noll gave an approximation for the phase variance (Noll, 1976), as

$$\Delta_J \approx 0.2944 J^{-\sqrt{3}/2} \, (D/r_0)^{5/3} \, [rad^2] \, . \tag{42}$$

Correcting an increasing number of Zernike modes changes the shape of the seeing disk in an unexpected way. Rather than narrowing the seeing disk in total, a diffraction limited spike appears on top of the seeing disk. This spike becomes more dominant with increasing number of corrected modes, until the seeing halo disappears for perfect correction. Since correcting the low orders does not affect r_0 very much it is intuitively understandable that the seeing disk, as λ/r_0, remains constant.

The image quality is usually expressed in terms of *Strehl ratio* that defines the peak of the point spread function normalised to the peak of the diffraction limited point spread function. The aberrations can be related to the Strehl ratio in a simple way using the Maréchal approximation (Born and Wolf, 1970). If the residual variance is smaller than about $\pi^2/4$ the Strehl ratio is approximated by

$$S = \exp(-(\Delta\phi)^2) \, . \tag{43}$$

For a numerical example, we assume an adaptive optics system that perfectly corrects the first 10 Zernike modes. The Fried parameter is $r_0 = 60$ cm which is typical in the near infrared and corresponds to a seeing value of $0.76''$. On a 3.5-m telescope the residual variance is $0.0401(D/r_0)^{5/3} = 0.76 \, rad^2$ and the Strehl ratio is 47%.

Expressing the wave-front as a Zernike polynomial the covariance matrix of the expansion coefficients $< a_i a_{i'} >$ plays an important role. This matrix can be calculated using the power spectrum of the phase fluctuations (Noll, 1976; Roddier, 1990b). It turns out that the covariance matrix is not perfectly diagonal. This means that when describing Kolmogorov turbulence with Zernike polynomials the Zernike modes are not statistically independent with the consequence that the wave-front reconstruction from the wave-front sensor data is sub-optimal. Noll found Karhunen-Loève functions to be more appropriate as they have a diagonal covariance matrix. Their disadvantage in practice is that they cannot be obtained in closed form. Using a method by (Roddier, 1990b) to approximate the Karhunen-Loève functions in terms of Zernike functions, Lane and Tallon (1992) have shown that when correcting more than about 20 modes the residual aberration starts decreasing faster when using Karhunen-Loève functions. In low order systems, this difference is negligible.

Instead of applying Karhunen-Loève functions for pure Kolmogorov turbulence one can also measure the covariance matrix by using actual atmospheric data and an

arbitrary set of polynomials. By diagonalising the measured covariance matrix one receives the Karhunen-Loève functions representing the optimum decomposition of the actual turbulent wavefront (Law and Lane, 1996; Kasper et al., 1999).

2.7.1. *Temporal evolution of Zernike modes*

Using the same formalism as for the analysis of the temporal characteristics of the image motion (Section 2.6) the temporal evolution of Zernike modes can be calculated (Noll, 1976; Roddier et al., 1993; Conan et al., 1995). The results are important for the specification of the bandwidth requirements of adaptive optics systems.

In the last section, the covariance matrix of the Zernike coefficients $< a_i a_{i'} >$ was calculated. Now we are interested in the temporal correlation of single Zernike coefficients $< a_i(t')a_i(t' + t) >$. Thus, equivalent to the calculation of the power spectrum of the image motion (Section 2.6) we determine a Zernike coefficient as the convolution

$$a_i(\rho, \theta) = \int_{\text{aperture}} \phi(\rho', \theta') Z_i(\rho - \rho', \theta - \theta')\rho d\rho' d\theta' . \tag{44}$$

At $\rho = 0$ and $\theta = 0$ this equation is identical to the calculation of the Zernike coefficient a_i (Equation 39) that can be used (see Noll, 1976) to calculate the variance of the Zernike modes (see Table II). The temporal covariance follows from the spatial covariance $< a_i(\rho', \theta') \, a_i(\rho' + \rho, \theta' + \theta) >$ by using the frozen turbulence hypothesis similar to the calculation of the image motion (Equation 34).

The resulting power spectra cannot be given in closed form. The numerical results were discussed by Roddier et al. (1993) and Conan et al. (1995), and they are briefly summarised here. The spectra show a dependence on the radial degree of the Zernike polynomial at low frequencies and a high frequency behaviour proportional to $f^{-17/3}$ that is independent of the Zernike mode. In the low frequency domain, polynomials with a radial degree of $n = 1$, Zernike tip and tilt (see Table I) decrease with $f^{-2/3}$. Higher order polynomials have a slightly different characteristic depending on their azimuthal dependence; all radially symmetric polynomials go with f^0, all others with f^0, with $f^{4/3}$ or with f^2 depending on the wind direction.

The transient frequency between the high and the low frequency regions can be approximated by

$$f_t^n \approx 0.3(n + 1)\hat{v}/D, \tag{45}$$

where n is the radial degree of the Zernike polynomials. The transient frequency is approximately equal to the bandwidth required to correct for the Zernike mode in an adaptive optics system.

Averaging the Zernike spectra for a given radial degree shows the mean behaviour for this degree. This behaviour can also be modelled when using a multi
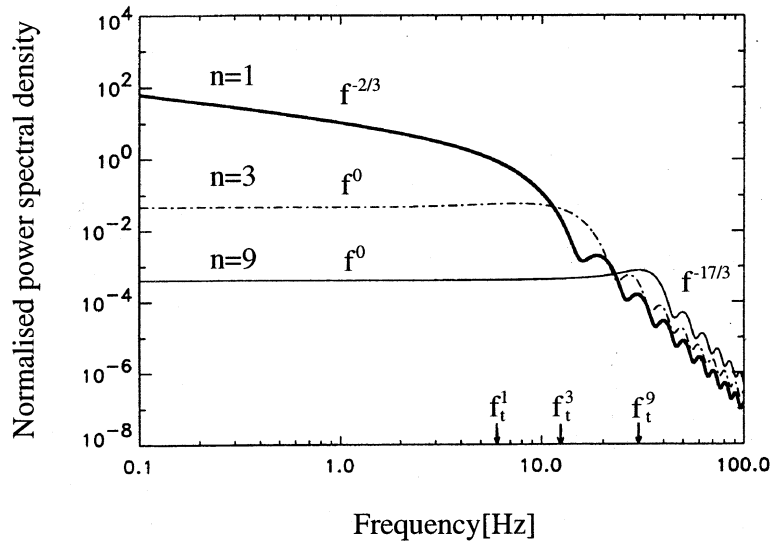
Figure 7. Zernike polynomial mean temporal power spectrum in a given radial degree *n* for *n* = 1, 3, 9. The spectra are normalised to the turbulence variance of one polynomial of the considered radial degree: $\hat{v}/D = 10$ Hz. The asymptotic power laws and the cutoff frequencies are indicated. The figure is taken from Conan et al. (1995).

layer model with different wind directions that is more realistic than the single layer approach (Conan et al., 1995). The curves are displayed in Figure 7. It shows that for $n > 1$ the power spectra are all proportional to f^0 at low frequencies. The curves are scaled in order to give the proper variance of the single modes (see Table II). It is interesting to note that at high frequencies the power spectra increase only very slowly with n. The increase in transient frequency f_t, and thus in bandwidth is partially compensated by the decrease in variance at higher radial degrees. Conan et al. (1995) argue that for a given degree of correction all modes have to be corrected with approximately the same bandwidth. Otherwise the residual variance from e.g. the tip-tilt correction could be larger than the uncorrected variance of a high order mode. This is particularly interesting for laser guide star systems, when the tip-tilt correction is decoupled from the high order correction. If the image motion is not corrected very accurately the quality achieved with the higher order corrections is easily destroyed. We will come back to this point in Section 3.3.

It is interesting to compare the high frequency behaviour of the image motion power spectrum (Equation (35)) that goes with $f^{-11/3}$ to the $f^{-17/3}$ decay of the Zernike tip-tilt terms. One can show (Glindemann and Rees, 1993), that the image centroid that usually characterises the image motion is the sum of Zernike-tilt, -coma and other higher order terms. The slower decrease can then be attributed to the sum of the single power spectra with increasing transient frequencies f_t. In the low frequency region the $f^{-2/3}$ dependence of the image motion power spectrum remains unchanged as all high order terms have much smaller contributions here.

3. Elements of adaptive optics systems

The requirements for the components of adaptive optics systems can be deduced from the discussion of imaging through turbulence in Section 2.

This section is organised as follows: Firstly, two different types of wave-front sensors will be presented and their performance at low signal levels will be discussed. Starting with the Shack-Hartmann sensor that is most commonly being used since it is conceptually simple and its properties are well understood, the curvature sensor is described next. Then, the mathematical principles for the reconstruction of the wave-front and the requirements for closed loop operation will be investigated. Finally, the technology of deformable mirrors will be presented.

3.1. WAVE-FRONT SENSING

3.1.1. *Shack-Hartmann sensor*

The Shack-Hartmann sensor divides the telescope aperture into an array of smaller subapertures, and a lenslet array is used to produce multiple images (see Figure 8). The centroid displacement of each of these subimages gives an estimate of the average wave-front gradient over the subaperture (Primot et al., 1990) that can be calculated using Equation (46). The important consequence is that the Shack-Hartmann sensor is achromatic – the image movement is independent of wavelength – and that extended sources can be used as long as they fit into the subimage boundary. The centroid, or first-order moment M, of the image intensity $I(u, v)$ with respect to the x-direction in the image, is related to the partial derivative of the wave-front in the subaperture by (Primot et al., 1990)

$$
\begin{aligned}
M_x &= \frac{\iint_{\text{image}} I(u, v)\, u\, du dv}{\iint_{\text{image}} I(u, v)\, du dv} \\
&= \frac{\lambda f}{2\pi} \iint_{\text{subaperture}} \frac{\partial \phi}{\partial x}\, dx dy = \frac{\lambda f}{2\pi} \int_0^{d/2} \int_0^{2\pi} \frac{\partial \phi}{\partial x} \rho d\rho d\theta \, ,
\end{aligned}
\tag{46}
$$

with f the lenslet focal length.

In practice, a Shack-Hartmann sensor is built by putting a lenslet array in the reimaged telescope pupil. The subimages from each subaperture are imaged onto a CCD camera. The size of the subimages has to be chosen such that the image motion even of extended sources does not drive the images outside of the subimage boundary. The single axis rms image motion can be calculated from the variance in Equation (33); it is

$$
\Delta\theta = 0.41(\lambda/r_0)(d/r_0)^{-1/6} [\text{arcsec}],
\tag{47}
$$

where d is now the diameter of the subaperture and λ/r_0 is the seeing in arcsec. $\Delta\theta$ is between 0.2 and 0.4 times the seeing and the peak-to-valley image motion
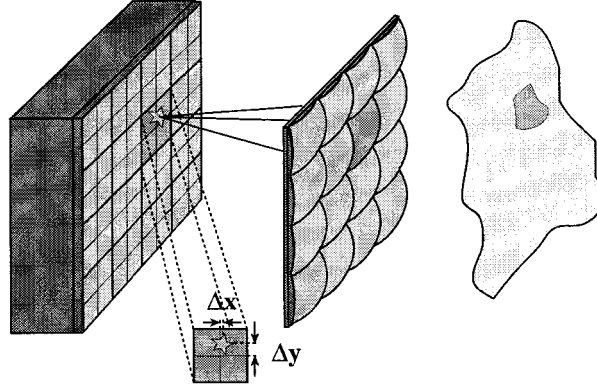
Figure 8. Measurement principle of a Shack-Hartmann sensor. The incoming aberrated wave is subdivided by the lenslet array and the image centroid in every subimage is shifted according to the average wave-front slope over the subaperture formed by the lenslet.

about six times this value. Thus, the size of the subimage should be at least three times the seeing. If the size of the extended sources is likely to be larger than this the subimage size has to be chosen accordingly. Even the solar surface can be used for wave-front measurement if a field stop and image correlation techniques are used to determine the wave-front gradients. If the subimage size is very large several sources can be observed independently allowing for isoplanatic effects to be measured (see Section 4) (Glindemann and Berkefeld, 1996).

The perfect information about the position of the subapertures with respect to the telescope aperture allows one to calculate the interaction matrix Θ_{sh} linking the image positions with the modes of the wave-front polynomial. However, this information might be difficult to obtain. Therefore a different approach was realised in ALFA*. Instead of calculating the subimage centroid positions for the Zernike modes (see the following example) the deformable mirror is driven to form these modes and the subimage centroids are then measured. This method is discussed in larger detail by Kasper et al. (2000).

The example of a $2{\times}2$ Shack-Hartmann sensor subdividing the aperture into four quarter circles explains the principle (Glindemann and Rees, 1994). The integration in Equation (46) has to be performed over the subapertures, i.e. for $\rho = 0$ to 1 and $\theta = 0$ to $\pi/2$ for the first subaperture. The centroid displacement in x for the first subaperture therefore becomes

$$M_{x1} = \frac{\pi}{2}a_2 + \frac{4}{\sqrt{3}}a_4 + \frac{2}{3}\sqrt{6}(a_5 + a_6) + \frac{3}{2}\sqrt{2}(a_7 + a_9) + \frac{\pi}{\sqrt{2}}a_8 + \ldots .$$

* ALFA is the laser guide star adaptive optics system of the 3.5-m telescope of the German-Spanish Astronomical Center on Calar Alto

As each lenslet yields two measurements, in x and in y, one obtains a total of eight gradients. The vector $\vec{M}$ containing the measured gradients, the interaction matrix Θ_{sh} and the vector $\vec{a}$ containing the coefficients of the Zernike polynomial form a matrix equation:

$$
\begin{pmatrix}
M_{x1} \\
M_{y1} \\
M_{x2} \\
M_{y2} \\
\cdot \\
\cdot \\
\cdot \\
M_{y8}
\end{pmatrix}
= \Theta_{\mathrm{sh}}
\begin{pmatrix}
a_1 \\
a_2 \\
a_3 \\
a_4 \\
\cdot \\
\cdot \\
\cdot \\
a_8
\end{pmatrix} .
\tag{48}
$$

For low light levels one has to consider two types of measurement errors that deteriorate the performance of the correction system: the photon noise σ_{ph}^2 and the read noise σ_r^2. These variances are given as variance of the wave-front phase due to photon noise and to read noise of the intensity measurement. Primot derived these quantities assuming that the seeing disk is approximately Gaussian and that it is centered (Primot et al., 1990).

Then the form of the phase variance due to signal photon noise is (Rousset, 1994)

$$
\sigma_{\mathrm{ph}}^2 = \frac{\pi^2}{2} \frac{1}{N_{\mathrm{ph}}} \left(\frac{\alpha_0 d}{\lambda} \right)^2 \ [\mathrm{rad}^2],
\tag{49}
$$

where N_{ph} is the total number of photoelectrons, α_0 the angular size of the image and d the diameter of the subaperture. In the diffraction limited case the image size α_0 is equal to λ/d and the variance is proportional to $1/N_{ph}$. In the case of a seeing limited point source with $\alpha_0 = \lambda/r_0$ it is

$$
\sigma_{\mathrm{ph}}^2 = \frac{\pi^2}{2} \frac{1}{N_{\mathrm{ph}}} (d/r_0)^2 \ [\mathrm{rad}^2].
\tag{50}
$$

The wave-front variance as a function of the detector read noise σ_d can be written in a similar fashion (Rousset, 1994)

$$
\sigma_r^2 = \frac{\pi^2}{3} f^2 N_{\alpha_0}^2 \left(\frac{\sigma_d}{N_{\mathrm{ph}}} \right)^2 \left(\frac{d}{r_0} \right)^4 \ [\mathrm{rad}^2],
\tag{51}
$$

with $N_{\alpha_0}^2$ the total number of pixels per Airy disk, and f the quotient between the area on the detector used for the centroid calculation, and the area of the seeing disk. (As long as the subaperture diameter is larger than r_0. This is always the case as the wave-front sensor operates in the visible with r_0 typically 10 cm.) If for

instance the (square) area on the detector is $(2'')^2$ in $0.7''$ seeing the quotient f is 10. The case of background photo noise is treated very similarly by replacing the detector read noise σ_d by the background noise σ_b (Rousset, 1994).

As already noted the wave-front sensor usually operates in the visible whilst the science camera works in the infrared. In order to convert the wave-front variances to the infrared they have to be multiplied by $(\lambda_{\mathrm{WFS}}/\lambda_{\mathrm{IR}})^2$. The number of pixels per Airy disk is determined by the optical design of the wave-front sensor. As the square of this number goes into the variance calculation it should be kept small.

Since the reconstruction of the phase is made through a linear process the noise of each subaperture measurement propagates linearly with

$$\sigma_{\mathrm{noise}}^2 = P(J) \left(\frac{\lambda_{\mathrm{WFS}}}{\lambda_{\mathrm{IR}}} \right)^2 \left(\sigma_r^2 + \sigma_{\mathrm{ph}}^2 \right), \tag{52}$$

where P(J) is the factor that describes the error propagation as a function of the number J of corrected modes. It depends on the properties of the system, like sensor and mirror geometry, number of sensors and actuators etc. Rigaut and Gendron (1992) have derived an expression for Zernike modes that is given as

$$P(J) \approx 0.34 \ln(J) + 0.10. \tag{53}$$

The error budget of a Shack-Hartmann sensor correcting for J modes can now be written as

$$\sigma_{\mathrm{st}}^2 = \Delta_J + \sigma_{\mathrm{noise}}^2, \tag{54}$$

where Δ_J is the wave-front fitting error after removing the first J Zernike modes given in Equation (41). The implications of the dynamic behaviour of the turbulence will be discussed in Section 3.3. It is interesting to note that the variance due to read noise ($\sigma_r^2 \propto (D/r_0)^4$) depends much stronger on the seeing conditions than $\Delta_J \propto (D/r_0)^{5/3}$ and $\sigma_{\mathrm{ph}}^2 \propto (D/r_0)^2$.

3.1.2. *Curvature sensor*

This technique was introduced by Roddier (1988). The adaptive optics system installed at the CFHT* in 1996 was the first large system to use a curvature sensor, and it has shown excellent performance. The obstacle preventing the wide spread use of this technique is the sophisticated theory behind the concept.

The curvature sensor relies on measuring the intensity distribution in two different planes on either side of the focus using the normalised difference between the distributions. This difference is a measure for the curvature of the wave-front in the telescope pupil and for the wave-front tilt at the aperture edge. The principle

---

* The CFHT is the Canada-France-Hawaii Telescope on Mauna Kea, Hawaii. It has a 3.6-m primary mirror.
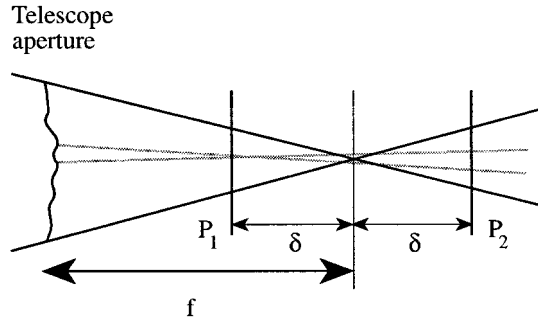
Telescope
aperture

Figure 9. Principle of the curvature sensor. The gray lines show the rays from a curved part of the wave-front that form a focus before the focal plane, leading to a local increase in intensity in plane P_1 and a decrease in P_2.

is sketched in Figure 9. The two intensity distributions are recorded in the two planes P_1 and P_2, a distance δ from the telescope focal plane. The figure displays the effect of a local curvature of the wave-front: the curved wave-front leads to a local excess of illumination in plane P_1 and to a lack of illumination at the corresponding position in P_2 as the light is spread out. The two planes of observation have to be far enough apart so that geometrical optics is a good approximation, i.e. $(f - \delta)\lambda/r_0 \leqslant r_0\delta/f$.

However, for extended sources and different degrees of correction the situation becomes more complicated. The local resolution of the wave-front measurement, given by the size of the subapertures in the Shack-Hartmann sensor, is determined by the size of the blur that is caused e.g. by the small piece of curved wave-front in Figure 9. If the separation δ is too small this blur is too small to be measured. Also, if the detector pixels are too large this blur cannot be resolved and the mode corresponding to aberrations of this size cannot be measured. Thus, the separation δ and the pixel size have to be adjusted according to the required degree of correction. An extended source has the same effect as a larger seeing disk, and the separation has to be adjusted accordingly. The conclusion is: for the measurement of high orders, δ must be larger than for low orders, and for extended sources, δ must be larger than for point sources (Rousset, 1994).

The normalised difference between the two intensity distributions is (Roddier, 1988):

$$c(x, y) = \frac{I_+(x, y) - I_-(x, y)}{I_+(x, y) + I_-(x, y)} \propto \left[\frac{\partial}{\partial \rho}\phi(\rho, \theta)\Psi - \nabla^2\phi(\rho, \theta) \right], \tag{55}$$

where $\nabla^2 = \frac{1}{\rho}\frac{\partial}{\partial\rho}(\rho\frac{\partial}{\partial\rho}) + \frac{1}{\rho^2}\frac{\partial^2}{\partial\theta^2}$ is the Laplacian operator representing the curvature of the wave-front. The wave-front radial tilt $\frac{\partial\phi}{\partial\rho}$ has to be weighted by an impulse distribution Ψ around the pupil edge. The advantage of the curvature measurement over the slope measurement in a Shack-Hartmann sensor is the very low correlation
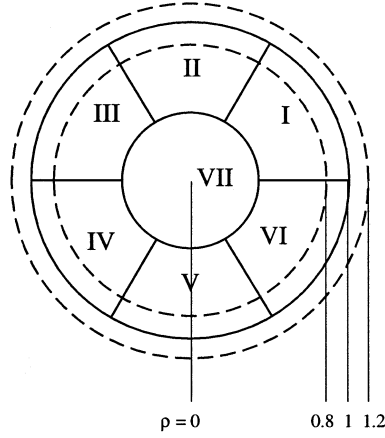
Figure 10. Sampling geometry for a low order curvature sensor. The illumination is integrated over each segment. The width of the impulse distribution Ψ is displayed by the dashed lines.

of the local curvature over the wave-front. Measuring statistically independent signals gives a better estimate of the wave-front (Roddier et al., 1991). Equation (55) is the irradiance transport equation for paraxial beam propagation providing a general description of incoherent wave-front sensing methods (Roddier, 1990a).

We have modelled a 7-element curvature sensor displayed in Figure 10 (Glindemann and Rees, 1994). Using the geometrical optics approximation $(f - \delta)\lambda/r_0 \leqslant r_0\delta/f$ one finds that δ is ± 90 mm for a f/35 beam on a 3.5-m telescope for $\lambda = 2.2\ \mu$m and $r_0 = 0.6$ m. Since we model a low order system we used $\delta = \pm 20$ mm. The signal in Equation (55) has to be integrated over the area of each segment where the width of the impulse distribution for the 6 edge segments has to be carefully adjusted. We have assumed that Ψ has a width of 20% of the pupil diameter and that it has a rectangular shape. Thus, we obtain the signal c_I at detector I in Figure 10 by integrating the curvature for $\rho = 0.5$ to 1 and $\theta = 0$ to $\pi/3$ and by integrating $\frac{\partial\phi}{\partial\rho}$ for $\rho = 0.8$ to 1.2 and $\theta = 0$ to $\pi/3$. The result is

$$c_I \propto 0.4\sqrt{3}\ a_2 + 0.4\ a_3 - 2.5\ a_4 + 1.489\ a_5 + 0.8598\ a_6 - 5.736\ a_7 \ldots .$$

One obtains a set of seven equations relating the signals of the sensors to the Zernike coefficients. This set of equations can be written in matrix form similar to Equation (48) as

$$\vec{c} = \Theta_c \vec{a}, \tag{56}$$

with $\vec{c}$ the vector containing the measured curvature and gradients for the edge segments, $\vec{a}$ the vector containing the coefficients of the Zernike polynomial and Θ_c the interaction matrix. A simple least-squares routine was used to solve this equation.

A comparative study between the 2×2 Shack-Hartmann sensor discussed in the previous section and the 7-element sensor discussed here has shown that the performance is very similar down to very low light levels (Glindemann and Rees, 1994; Rousset, 1994)

The measurement errors of the curvature sensor were investigated by Roddier et al. (1991). He found that in open loop operation the error propagation coefficient $P(J)$ (Equation (53)) increases with J and not with $\ln(J)$. However, in closed loop operation there is no significant difference between the two methods (Roddier, 1995). Thus, curvature sensor systems are as well suited for high order correction as Shack-Hartmann systems. As a consequence, the adaptive optics system of the VLT* Interferometer will have a 60-element curvature wavefront sensor at each 8-m telescope (Bonaccini et al., 1998).

3.2. WAVE-FRONT RECONSTRUCTION

In the last section, we have assumed that the modes of a polynomial, in our example the Zernike modes, are reconstructed from the information obtained by the wave-front sensor. Apart from this modal reconstruction of the wave-front there exists also the zonal approach where the error in e.g. each subimage of a Shack-Hartmann sensor is minimised by tilting the wave-front in the subaperture. In a curvature sensor system this approach is even more intuitive in combination with a bimorph mirror (see Section 3.4). Here, the curvature of the mirror surface is changed by applying a voltage to the mirror actuator and, in principle, the measured curvature signal from a single detector element can be hard-wired to the corresponding actuator of the bimorph mirror (Roddier et al., 1991).

In both cases the local piston of the wave-front elements in each subaperture has to be treated separately in order to smoothly model the wave-front. This requires some sophisticated reconstruction techniques (Rousset, 1994). Together with the high accuracy that is required in the opto-mechanical alignment to ensure a precise correspondence between the wave-front sensor elements and the deformable mirror actuators, the zonal approach becomes less attractive than the modal approach.

The matrix equation for the modal reconstruction $\vec{M} = \Theta_{sh}\vec{a}$ (Equation 48) connecting the coefficients of the Zernike modes $\vec{a}$ with the wave-front slopes $\vec{M}$ can be solved by a least-squares approach:

$$\vec{a} = (\Theta_{sh}^T \Theta_{sh})^{-1} \Theta_{sh}^T \vec{M}. \tag{57}$$

The product of matrices $(\Theta_{sh}^T \Theta_{sh})^{-1} \Theta_{sh}^T$ is called reconstructor matrix. This method can be extended to include the noise characteristics by adding a noise vector to the vector of slopes

$$\vec{M}_n = \vec{M} + \vec{N}. \tag{58}$$

---

* The ESO Very Large Telescope Interferometer located on Cerro Paranal in northern Chile consists of four 8-m telescopes separated by up to 130 m and of three 1.8-m telescopes separated by up to 200 m.

To solve this equation the covariance matrix of the noise $< \vec{N}\vec{N}^T >$ has to be calculated. Since the two noise sources, the photon noise and the read noise, are statistically independent for each subaperture the covariance matrix is diagonal. If the noise variance of each subaperture is the same and equal to σ^2_{noise} the result of the least-square minimisation can be written as (see e.g. Melsa en Cohn, 1978)

$$\vec{a} = (\Theta^T_{\text{sh}}\Theta_{\text{sh}} + \sigma^2_{\text{noise}} < \vec{a}\vec{a}^T >^{-1})^{-1}\Theta^T_{\text{sh}}\vec{M}, \tag{59}$$

where $< \vec{a}\vec{a}^T >$ is the covariance matrix of the Zernike coefficients This technique to reconstruct the wave-front is also called *maximum likelihood technique* as by determining $\vec{a}$ one maximises the probability of producing the measurements $\vec{M}$. This method has recently been improved by implementing knowledge about the correlation of the slopes between the subapertures (Sallberg et al., 1997).

The coefficients $\vec{v}$ of the polynomials of the deformable mirror (the mirror modes) are related to the Zernike coefficients $\vec{a}$ through an additional interaction matrix so that a new interaction matrix can be calculated linking the slope measurements $\vec{M}$ directly with $\vec{v}$. The formalism is the same as above, with the exception that it might be extremely difficult to calculate the inverse of the covariance matrix $< \vec{v}\vec{v}^T >$ for a non-orthonormal set of mirror modes. If the mirror modes do not exactly match the surface of the mirror the maximum likelihood technique no longer represents the best estimate of the wave-front (Roggemann and Welsh, 1996). The minimum-variance method can be used to circumvent this problem (Wallner, 1983). Here, in order to maximise the image intensity the variance of the residual wave-front aberrations are minimised incorporating the mirror influence function. The practical drawback is that accurate knowledge of the wave-front and noise statistics, and of the mirror influence function are required.

3.3. CLOSED LOOP OPERATION

So far, the properties of wave-front sensors have been discussed for the static case of a single measurement. In order to investigate the performance of adaptive optics systems the dynamic behaviour of turbulence has to be considered. In Sections 2.6 and 2.7, the temporal characteristics of image motion and of the Zernike modes have been discussed. These properties are used in the following investigation of the dynamic requirements of adaptive optics systems.

Two parameters have to be adjusted according to the number of modes that are corrected: the gain and the bandwidth. The gain should be different for each mode depending on the accuracy of the measurement that can be determined experimentally.

The required bandwidth for full correction was given by Greenwood (1977). He assumed a system that in the static case corrects the wave-front perfectly, and that all aberrations are caused by the finite bandwidth of the control system. He then used the power spectrum $\Phi_t(f)$ of the phase fluctuations of the wave-front (Equation 28) and applied the transfer function $T(f)$ to calculate the correction

bandwidth f_G that was subsequently called the Greenwood frequency. Using the single dominant layer approximation it is

$$f_G = 0.43 \frac{\hat{v}}{r_0}. \tag{60}$$

The residual variance of the wave-front can then be calculated as

$$\sigma_G^2 = (f_G/f_{3dB})^{5/3} [\text{rad}^2] . \tag{61}$$

If the servo bandwidth f_{3dB} of the closed loop system is chosen equal to f_G the variance is 1 rad^2 which is equivalent to a Strehl ratio of about 35%.

This variance has to be compared to the residual variance after correcting e.g. 50 Zernike modes perfectly. Using Equation (42), one finds that it is $\Delta_{50} = 0.25 \text{ rad}^2$ in $0.9''$ seeing, corresponding to a Strehl ratio of 77%. Although Greenwood's assumption of a perfect system cannot be compared easily to the case of removing only a limited number of Zernike modes – leaving a residual phase variance even for infinite bandwidth – it is clear that the Greenwood frequency with the residual variance of 1 rad^2 is too small for a good correction.

In the case of a laser guide star adaptive optics system the image motion has to be measured with a natural guide star (see Davies et al., 2000). If it is the goal to reduce the single axis rms image motion $\Delta\theta$ to $0.25\lambda/D$ the tracking bandwidth is (see for example Glindemann, 1997)

$$f_{\text{h.o.,T}} = 0.25 \frac{\hat{v}}{r_0}. \tag{62}$$

Tyler (1994) investigated pure Zernike tilt and the centroid tilt separately, and he presented a similar result.

The subsequent variance of the wave-front phase due to the residual image jitter alone is

$$\sigma_{\text{h.o.T}}^2 = (f_{\text{h.o.T}}/f_{3dB})^{5/3} 0.33 \, [\text{rad}^2]. \tag{63}$$

The very simple assumptions that lead to these results make it impossible to draw far reaching conclusions. However, it is fair to say that the tip-tilt system has to be run at almost the same frequency as the higher order system in order to add an acceptable amount to the variance of the wave-front. Conan et al. (1995) came to a very similar conclusion discussing the temporal power spectra of the Zernike modes that are displayed in Figure 7.

If for example the effective wind speed $\hat{v}$ is 15 m s^{-1} and if r_0 is 60 cm which is equivalent to $0.76''$ seeing at $2.2 \, \mu$m the bandwidth for full correction according to the Greenwood criteria is $f_G = 11$ Hz, and the required tracking bandwidth is $f_{\text{h.o.,T}} = 6$ Hz. The respective tracking frequencies are about 110 and 60 Hz. It

should be emphasised that this can only give an idea about the order of magnitude since the adaptive optics system is not perfect as Greenwood assumed, and, as noted above, since a residual variance of $1\,\text{rad}^2$ is too large. In practice one can start at about 2–4 times the Greenwood frequency and determine the optimum bandwidth by examining the image quality achieved.

3.3.1. *Error budget – limiting magnitude*
We can now write down the error budget of an adaptive optics system with a Shack-Hartmann sensor:

$$\sigma^2 = \Delta_J + \sigma_{\text{noise}}^2 + \sigma_{\text{bw}}^2, \tag{64}$$

with Δ_J the fitting error that represents the wave-front variance due to the un-corrected Zernike modes, σ_{noise} the measurement noise that is due to photon and read-noise (see Equations 52 and 53), and σ_{bw} the error due to finite bandwidth.

The error due to the finite bandwidth was discussed in the last section and given to be

$$\sigma_{\text{bw}}^2 = \sigma_G^2 = (f_G/f_{\text{3dB}})^{5/3}\text{rad}^2, \tag{65}$$

where the Greenwood frequency is $f_G = 0.43\,\hat{v}/r_0$. A numerical example will illuminate the situation.

We assume a situation when the seeing is $0.76''$ in the near infrared at $2.2\,\mu\text{m}$ on a 3.5-m telescope. The Fried parameter is then $r_0 = 0.6$ m. A Shack-Hartmann sensor, operating in the visible with $\lambda_{\text{WFS}} = 0.5\,\mu\text{m}$ and 5×5 subapertures ($d = 0.7$ m) is used to correct for 15 Zernike modes. In the table the seeing parameters are summarised:

Wavelength	$0.5\,\mu\text{m}$	$2.2\,\mu\text{m}$
Seeing	$1''$	$0.76''$
d/r_0	7	1.1

The discussion starts with the fitting error, i.e. the best variance that we can theoretically achieve if correcting 15 Zernike modes. It is $\Delta_J = 0.028(D/r_0)^{5/3} = 0.56\,\text{rad}^2$ corresponding to a Strehl ratio of 57%. If we want to add less than $0.2\,\text{rad}^2$ to the variance, i.e. if the Strehl is to stay above 45%, one can for a first iteration allow $0.1\,\text{rad}^2$ for the noise error and equally $0.1\,\text{rad}^2$ for the bandwidth error. The Greenwood formula can be used to estimate the required bandwidth and then the star magnitude can be determined that provides enough photons to have less than $0.1\,\text{rad}^2$ for the noise error.

With $\hat{v} = 15$ m s^{-1} and $r_0 = 0.6$ m the Greenwood frequency is 11 Hz. Since we want to add less than $0.1\,\text{rad}^2$ to the variance the bandwidth f_{3dB} has to be 44 Hz, and, thus, the sampling rate of the Shack-Hartmann sensor has to be 10 times the bandwidth, i.e. about 450 Hz. The exposure time is then about 2 msec.

The measurement noise in a Shack-Hartmann sensor is given by Equations (50) and (51). Assuming a wave-front sensor with a pixel size of $0.72''$ and a subimage size of $2''$, and correcting $J = 15$ Zernike modes ($P(J) \approx 1$), yields

$$\sigma_{\text{noise}}^2 = \left(40\frac{\sigma_d}{N_{\text{ph}}}\right)^2 + \frac{12}{N_{\text{ph}}} \, [\text{rad}^2] \, . \tag{66}$$

If the read-noise is $\sigma_d = 5$ electrons, which is typical for CCD cameras we need about 600 photons per subaperture in 2 msec to reduce the additional variance to $0.1\,\text{rad}^2$. This corresponds to a star with $m_V = 10$, which is a realistic number for the set of parameters used here. If the requirements for the bandwidth are relaxed the variance σ_{bw}^2 increases with $f_{\text{3dB}}^{-5/3}$ and σ_{noise}^2 decreases with N_{ph}^2 as long as the second term in Equation (66), remains small. Thus, reducing the bandwidth by a factor of two increases the σ_{bw}^2 by a factor of 3 but it reduces the read noise by a factor of 4 resulting in a net gain in performance. However, since the concept of the Greenwood frequency is fairly crude and one should not overestimate the significance of the calculated values for small changes.

One parameter that has not been treated so far is the isoplanatic angle that determines the maximum distance between the object and the guide star. This depends heavily on the degree of correction and the layer structure of the atmosphere. Rigaut (1994) has investigated this quantity and found that, depending on the tolerated additional variance values between $10''$ and $30''$ can be expected in the near infrared. If a guide star of 10th magnitude has to be no more than $30''$ from the astronomical object the number of objects that fulfill this requirement is very small. Then the sky coverage is on average below 0.1% on a 4-m class telescope.

However, if a laser guide star can be placed anywhere in the sky the situation changes dramatically. Only the tip-tilt correction relies on a natural guide star, and here the requirements are much relaxed compared to the full correction. Using the full aperture D with $D/r_{0,\lambda=0.5\,\mu m} = 35$ for the calculation of the measurement noise σ_{noise}^2 one obtains

$$\sigma_{\text{noise}}^2 = \left(210\frac{\sigma_d}{N_{\text{ph}}}\right)^2 + \frac{312}{N_{\text{ph}}} \, [\text{rad}^2] \, . \tag{67}$$

If the tolerated additional variance is $0.1\,\text{rad}^2$ and the read noise $\sigma_d = 5$ electrons, 3000 photons per exposure are required.

The bandwidth f_{3dB} for tip-tilt correction with $\sigma_{\text{h.o.,T}}^2 = 0.1\text{rad}^2$ can be calculated using Equation (63), yielding $f_{\text{3dB}} = 0.5 \, \hat{v}/r_0 = 12.5$ Hz, resulting in a tracking frequency of 125 Hz and an exposure time of 8 msec. Here, the tip-tilt system has to run faster than for pure tip-tilt tracking (Glindemann, 1997a) because the error has to be reduced to the absolute value of $0.1\,\text{rad}^2$ independent of seeing conditions. 3000 photons per 8 msec exposure time correspond to a magnitude of about $m_V = 13$. This limiting magnitude and the larger isoplanatic angle increase
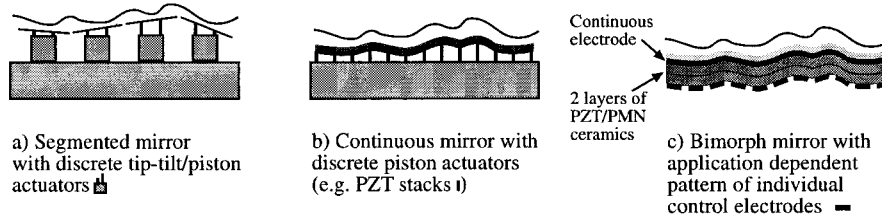
Figure 11. Three classes of deformable mirrors: (a) a segmented mirror with tip-tilt/piston actuators behind each segment, (b) continuous facesheet mirrors with individual piston actuation, and (c) an example of a bimorph (metal/PZT or metal/PMN) mirror.

the sky coverage in the K-band to about 15% at the galactic pole and about 95% at the galactic equator.

The cone effect, however, slightly deteriorates the achievable Strehl ratio. Since the light of the laser guide star does not travel the same light path as the natural star light there is a fraction of the turbulence that cannot be corrected. This reduction in Strehl ratio is less than 20% in average seeing conditions on a 4-m class telescope but it goes up to 50% on an 8-m telescope.

3.4. Deformable mirrors

The earliest developments of deformable mirrors aimed at TV projection systems in the early 1950's. In the so-called Eidophor system, a mirror in a vacuum chamber is covered with a thin layer of oil upon which a modulated beam from an electron gun is deposited in a rastered pattern. Local forces of surface repulsion are induced forming transient changes in the slope of the oil film. The wave-front is then locally tilted by refraction in traversing the film. The optical system of the TV projector blocks the tilted beam, and the point on the mirror remains dark in projection. Bright spots appear in the projected image of the mirror where the oil film is flat. The TV image is modulated onto the mirror by modulating the beam from the electron gun similar to the process of forming an image with a cathode ray tube.

For the application in adaptive optics systems the ability of the Eidophor mirror to shape the wave-front with local tilts was used. Babcock (1953) suggested to use this mirror in his proposal for an adaptive optics system. However, the technological problems at that time were too large to actually build the system.

Today, there are mainly three classes of deformable mirrors displayed in Figure 11: The *segmented mirror* with single tip-tilt/piston elements and two mirror types with a continuous surface, the *continuous mirror* where an array of actuators behind the mirror surface pushes and pulls the mirror by applying a force perpendicular to the surface, and the *bimorph mirror* where voltages applied between the continuous electrode and the control electrodes change the curvature of the mirror (for a review, see Ribak 1994).

Segmented mirrors have a number of advantages over continuous mirrors: the segments can be moved independent of each other, they can be replaced easily,

and the single segments can be combined to form rather large mirrors. In the section on wave-front sensors (Section 3.1) it was discussed that by associating each sub-aperture of a Shack-Hartmann sensor to a segment of the mirror the high order adaptive optics systems consist basically of tip-tilt systems that are run in parallel. Although this is appealing because of its conceptual simplicity, in addition to the single segment tip-tilt correction, one has to process the data to obtain the piston signals that are necessary to reconstruct a continuous wave-front. Also the alignment between the subapertures of the Shack-Hartmann sensor and the single segments has to be very precise. The disadvantages of segmented mirrors include problems with diffraction effects from the individual segments and the intersegment alignment. In infrared applications the gaps between the segments can be the source of infrared radiation that deteriorates the image. Only few adaptive optics systems with segmented mirrors have been built for solar (Acton and Smithson, 1992) and stellar (Doel et al., 1990) astronomy.

Bimorph mirrors have their name from the structure that controls their shape. Piezoelectric bimorph plates usually consist of either a metal plate and a piezoelectric plate (e.g. PZT or PMN ceramic) or of two piezoelectric plates which are bonded together. The latter layering is often called the *standard bimorph* whilst the first one is sometimes called *unimorph* or *monomorph*. A piezoelectric bimorph operates similar to a bimetallic strip in a thermostat. In a typical serial configuration one part of the bimorph expands and the other contracts when a voltage is applied between the two parts. The result is a bending of the entire structure. As shown in Figure 11c discrete bimorph (or bending) actuators are created by attaching control electrodes to the bottom side of the bimorph structure. The pattern of the control electrodes can be such that it corresponds to the geometry of a curvature sensor (see Figure 10). The local radius of curvature of the bimorph mirror changes proportional to the applied voltage (on a given control electrode). This behaviour make bimorph mirrors the natural counterparts of the curvature sensor. As noted in Section 3.1, it was discussed to feed the signal from the curvature sensor directly to the bimorph mirror (Roddier et al., 1991). This design is similar in its conceptual simplicity to the idea of using a mirror segment for each subaperture of a Shack-Hartmann sensor. However, the requirements for the optical alignment are similar. The bimorph mirrors that are commercially available used to have only a low number of actuators, e.g. the bimorph mirror in the CFHT adaptive optics system has 19 actuators (see Section 3.1). In the meantime, bimoroph mirrors with 36 actuators are available and tested in a curvature sensor system (Graves et al., 1998), and mirrors with 60 actuators are being designed.

Piezo-electric mirrors, i.e. continuous mirrors with an array of piezo-electric actuators expanding perpendicular to the mirror surface (Figure 11b) are in widespread use now. They are available with up to 350 actuators, and the technology is well tested and very reliable. They were developed originally to project high power laser beams on military targets when segmented mirrors produce too much scattered light (Tyson, 1998). The typical voltage that is required to move the ac-

tuators is below 100 V, the bandwidth is in the kHz range, and the typical stroke is in the 5 μm range. Whilst this is sufficient for high order correction the tip and tilt induced by the turbulence requires a larger tilting angle so that an extra tip-tilt mirror is needed. Some manufacturers are now using electrostrictive material like a lead-magnesium-niobate (PMN) crystal that is similar to the piezo-electric lead-zirconate-titanate (PZT) ceramics, but that displays a smaller hysteresis and a better motion control.

Both types of continuous surface mirrors avoid the diffraction effects associated with the single segments and the intersegment alignment problem. Here, the problems arise from the complexity of the algorithm to control the mirror surface as the actuators are not allowed to move independent of each other. If one actuator is set to the maximum voltage its next neighbour must not be set to the minimum voltage. Otherwise the mirror surface would be damaged. Also, changing the voltage of a particular actuator usually affects the shape of the mirror surface at the location of its neighbours.

There are several new developments ranging from very large deformable mirrors that can replace the telescope secondary (Salinari et al., 1993), to extremely small units that are based on microelectronical manufacturing methods (Vdovin and Sarro, 1995). A completely different class of wave-front actuation is represented by the liquid crystal half-wave phase shifter especially suitable for narrow band applications (Love et al., 1995). The LBT* will be equipped with an adaptive secondary with 1000 actuators that has a diameter of 870 mm and a thickness of 2 mm. It is discussed to use an actuator design based on loudspeaker technology where the actuator motion is provided by voice coils. The advantage of the design with an adaptive secondary is the conceptual elegance and the low number of reflections that improve both the optical throughput and the infrared background (Hill, 1996).

4. Outlook – multi-layer adaptive optics

The size of the corrected field of view of an adaptive optics system can be increased by using multiple deformable mirrors correcting multiple turbulent layers individually (see Figure 12) (Beckers, 1988). In recent years, several groups have explored methods of measuring the turbulent layers individually, and the possible improvements in performance both with respect to increasing the isoplanatic angle and reducing the cone effect on large telescopes have been investigated (Johnston and Welsh, 1994; Ribak et al., 1996; Berkefeld, 1998). In the following, we discuss a new method for measuring separately the turbulence in multiple atmospheric layers by combining intensity measurements like in a curvature sensor with wave-front gradient measurements in a Shack-Hartmann sensor (Glindemann and Berkefeld, 1996).

---

* The Large Binocular Telescope consists of two 8.4-m telescopes separated by 14.4 m (center to center). The Telescope is currently under construction on Mount Graham in Arizona, U.S.A.
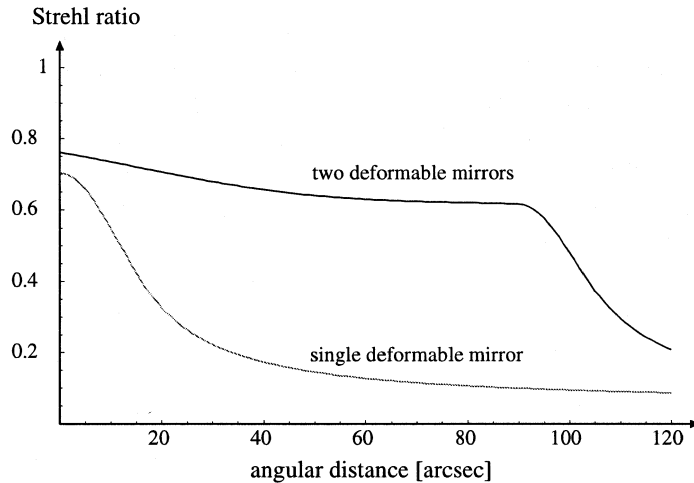
Figure 12. Strehl ratio as a function of angular distance from the optical axis for conventional adaptive optics with a single deformable mirror (grey curve) and for multi-layer adaptive optics with two deformable mirrors (black curve). The calculations were performed using a measured C_n^2 profile at Calar Alto (Klückers et al., 1997). The figure is taken from Berkefeld (1998).

The problem of measuring the atmospheric turbulence can be reduced to imaging a phase object, i.e. an object affecting only the phase of the wave-front. This is a common problem in microscopy, and defocusing is an old cure. Then, the phase object that is invisible in the focused image shows up in the intensity distribution. If the phase varies only slightly, ($\phi(x) \ll 1$) the image intensity is proportional to the curvature of the phase distribution. Thus, the scintillation on the ground could be used for an estimate of the high altitude layers. In order to reconstruct the phase distribution completely, the intensity distribution has to be measured in two planes positioned symmetrically to the image plane of the phase object. The curvature sensor is based on this idea.

To simplify the explanation, we start with two dominant layers that carry the bulk of the turbulence. Then, the intensity distribution $I_1(x_1)$ in the conjugate plane L_1' of layer L_1 in Figure 13 would be determined solely by the turbulence in layer L_2. The turbulence in layer L_1 has no effect on the intensity distribution in its image plane, L_1'. Vice versa, the intensity distribution in L_2' is caused only by the turbulent layer in L_1.

Assuming that the phase variation is weak, with $\phi(x) \ll 1$, the complex amplitude immediately behind layer L_1 can then be written as

$$u_1(x_1) = 1 + i\phi_1(x_1).$$

The wave-front amplitude $u_2^-(x_2)$ immediately before L_2 is the Fresnel diffraction pattern of the turbulence in L_1, which is approximately

$$u_2^-(x_2) = 1 + i\phi_1(x_2) + \frac{s_{12}}{2k}\frac{\partial^2\phi_1(x_2)}{\partial x_2^2}, \tag{68}$$

with $k = 2\pi/\lambda$. The turbulence in layer L_2 adds to the imaginary part of $u_2^-(x_2)$ yielding

$$u_2(x_2) = 1 + i\,(\phi_1(x_2) + \phi_2(x_2)) + \frac{s_{12}}{2k}\frac{\partial^2\phi_1(x_2)}{\partial x_2^2}. \tag{69}$$

Calculating the wave-front in image space, one has to be careful to include the phase disturbances of both layers. Thus, the complex amplitude $u_2'(x_2')$ in L_2' is, neglecting imperfections of the imaging optics, identical to $u_2(x_2)$ in L_2. However, to calculate the wave-front in L_1' the turbulence in L_2 has to be considered. One then finds that the wave-front phase both in planes L_1' and L_2' is equal to the sum of the phases, $\phi_1 + \phi_2$, and that the intensity in L_1' resp. L_2' can be written as

$$I_1'(x_1') = 1 - \frac{s_{12}'}{2k}\frac{\partial^2\phi_2(x_1')}{\partial x_1'^2} \quad \text{and}$$

$$I_2'(x_2') = 1 + \frac{s_{12}'}{2k}\frac{\partial^2\phi_1(x_2')}{\partial x_2'^2}$$

The intensity distribution in L_1' is unaffected by ϕ_1 and the intensity distribution in L_2' is unaffected by ϕ_2. Using the difference of the intensity distributions like a curvature sensor yields the second derivative of the sum of the phases. This is the result of a measurement with a curvature sensor neglecting the wave-front radial tilt.

Using Shack-Hartmann sensors in both planes L_1' and L_2', the resulting phase $\phi_1 + \phi_2$ of the wave-front is measured in each plane by determining the wave-front tilt in each subaperture. Additionally, the intensity distribution can be measured in both planes by integrating over each subaperture of the lenslet array. The normalised signal $I_1' - I_2'/I_1' + I_2'$ is the quotient of the second derivative of the sum and of the difference of the phases. As the sum of the phases is measured directly, the difference of the second derivatives can be determined and, thus, the phase curvature in both layers.

The isoplanatic angle can now be enlarged by observing multiple stars with the Shack-Hartmann sensor as displayed in Figure 13. The phase as well as the intensity distribution can be measured for each star individually. Then, the information about the different layers can be stitched together to steer the deformable mirrors in the conjugate planes of L_1 and L_2.

Before placing the Shack-Hartmann curvature sensors in the conjugate planes of the turbulent layers their altitude has to be determined by e.g. using a method suggested by Vernin and Roddier (1973).
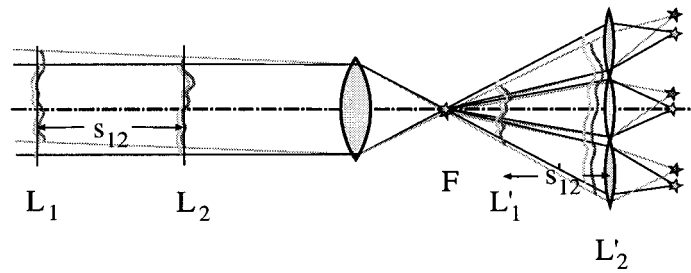
Figure 13. Illustration of the multiplexer mode of the Shack-Hartmann curvature sensor. For the sake of clarity only one lenslet array is displayed. In each subimage the total intensity and the centroid position can be measured separately and, thus, different patches of the wave-front can be reconstructed.

So far, the discussion has been restricted to two layers. If the turbulence profile indicates multiple strong layers there has to be a Shack-Hartmann curvature sensor in each conjugate plane of those layers. The position of the deformable mirrors can be adjusted to correspond to the conjugate planes of the layers. The number of deformable mirrors in a real system is obviously fixed. However, the system could be designed with several deformable mirrors using only the required number.

The isoplanatic angle is limited by the separation of the stars used for the measurement of the turbulence. The practical limitation is given by the field of view of each subimage of the Shack-Hartmann sensor. To correct 30 Zernike modes one needs about 7×7 subapertures each of which with a field of view of $30 \times 30''$. Then, with a pixel scale of roughly $0.7''$ every subimage has a size of 42×42 pixels, and the total size of the CCD is 300×300 pixels.

5. Conclusions

We have discussed effects of imaging through turbulence and methods to improve the reduced image quality with adaptive optics. The detailed description of existing adaptive optics systems has shown that the technical requirements are met by current technology. There are now about 10 telescopes in the world where adaptive optics is used on a more or less regular base. One can expect that this technology will mature considerably over the next few years, and that the impact on astronomical research will become significant. In particular the new 10-m class telescopes that will all be equipped with adaptive optics will contribute to the scientific progress since diffraction limited images from these telescopes means a factor of 20 to 50 improvement over seeing limited images.

On a more modest scale, simple tip-tilt systems improve the peak intensity by 70 to 300% and the FWHM by about $0.2''$ in the near infrared, increasing the scientific output of a telescope without any significant disadvantage. Thus, it is very worthwhile to equip infrared telescopes with tip-tilt systems.

The limit of resolution is an area where large ground based telescopes are superior to observations from space telescopes since the limit for the size of a monolithic mirror in space is considerably below 10 m. Other advantages of ground based telescopes are cost, lifetime, and flexibility as improvements or new instruments can be fitted easily.

If it comes to field of view and sky coverage, so far, the space telescopes have an advantage over observations from the ground. We have discussed methods to increase the corrected field of view of ground based observations by using multi-layer adaptive optics, and to increase the sky coverage by creating laser guide stars. For multi-layer adaptive optics one has to tackle the problems of separating the influence of single turbulent layers on the imaging process, and of applying the correction to the proper layers with multiple deformable mirrors. Laser guide stars provide a method to determine the aberrations caused by the turbulence with the exception of the wave-front slope. Although this already increases the sky coverage drastically one has to be able to deduce the tip-tilt information from the laser guide star in order to achieve 100% sky coverage. The research has to concentrate on these two areas to make observations from the ground competitive with space observations.

Since angular resolution is of key importance in most areas of astronomical research the desire for higher resolution does not stop at 10 m apertures. However, rather than envisioning larger monolithic telescopes, interferometer arrays are planned and tested, coherently switching together the light from single telescopes. Then, the limit of resolution is given by the longest baseline. The most challenging projects in this area are the interferometric connection of the two Keck Telescopes, the VLTI connecting eventually the four Very Large Telescopes in Paranal, Chile and the interferometric mode of the LBT. Each of the single 8-10 m apertures requires adaptive optics to increase the peak intensity and the accuracy of the measurement. The coherently combined beams display a fringe pattern that moves around randomly depending on the wave-front slope between the single apertures. This cannot be corrected for by the adaptive optics systems in each telescope. Similar to the problem of the tip-tilt measurement with a natural guide star in a laser guide star system one needs a natural guide star to stabilise the fringe motion.

Here, one faces the same problems as with single telescope adaptive optics. The correction frequency for fringe tracking is affected by the telescope baseline and by the observing wavelength. This determines the limiting magnitude. If the scientific object is not bright enough to serve as a guide star there has to be a star of suitable brightness usually within a few arcseconds of the scientific object. Then, one can use the guide star to stabilise the fringe motion, and one can integrate on the scientific object. Increasing the angle between the object and the guide star is most desirable since it improves the sky coverage. This technique has to be mastered in order to make telescope interferometers useful. The experience with adaptive optics systems is a stepping stone to solving these problems.

References

Acton, D. S. and Smithson, R. C.: 1992, 'Solar imaging with a segmented adaptive mirror', *Appl. Opt.* **31**, 3161–3169.

Alloin, D. M. and Mariotti, J.-M. (eds.): 1994, *Adaptive Optics for Astronomy*, Vol. C423, NATO Advanced Study Institute Series, Kluwer Academic Publishers.

Babcock, H. W.: 1953, 'Possibility of compensating astronomical seeing', *Publ. Astron. Soc. Pac.* **65**, 229.

Beckers, J. M.: 1988, 'Increasing the Size of the Isoplanatic Patch with Multiconjugate Adaptive Optics', in M. H. Ulrich (ed.), *Proceedings of the ESO Conference on Very Large Telescopes and their Instrumentation*, Vol. 30, Garching, Germany, pp. 693–703.

Beckers, J. M.: 1993, 'Adaptive optics for astronomy: Principles, performance and applications', *Annual Review of Astronomy and Astrophysics* **31**, 13–62.

Berkefeld, T.: 1998, *Untersuchungen zur Messung und Korrektur einzelner Schichten der Erdatmosphäre*, Dissertation, Universität Heidelberg.

Bonaccini, D., Rigaut, F., Glindemann, A., Dudziak, G., Mariotti, J.-M. and Paresce, F.: 1998, 'Adaptive Optics for ESO VLT-Interferometer', in *Adaptive Optical Systems Technologies*, Proc. SPIE 3353, pp. 224–232.

Born, M. and Wolf, E.: 1970, *Principles of Optics*, Pergamon Press, Oxford.

Clifford, S. F.: 1968, 'The Classical Theory of Wave Propagation in a Turbulent Medium', in: J. W. Strobehn (ed.), *Laser Beam Propagation in the Atmosphere, Topics in Applied Physics*, Vol. 25. Springer-Verlag, Berlin, pp. 9–43.

Colavita, M. M.: 1990, 'Design Considerations for Very Long Baseline Fringe-Tracking Interferometers', in J. Breckinridge (ed.), *Amplitude and Intensity Interferometer*, Proc. SPIE 1237, pp. 80–86.

Conan, J. M., Rousset, G. and Madec, P. Y.: 1995, 'Wave-front temporal spectra in high-resolution imaging through turbulence', *J. Opt. Soc. Am.* **A12**, 1559–1570.

Davies, R. et al.: 2000, 'The ALFA laser guide star: operation and results', *Experimental Astronomy* **10**, 103–121 (this issue).

Doel, A. P., Dunlop, C. N., Major, J. V., Myers, R. M., Purvis, A. and Thompson, M. G.: 1990, 'Stellar Image Stabilisation using Piezo-Driven Active Mirrors', in L. D. Barr (ed.), *Advanced Technology Optical Telescopes IV*, Proc. SPIE 1236, pp. 179–192.

Fried, D. L.: 1965, 'Statistics of a geometric representation of wavefront distortion', *J. Opt. Soc. Am.* **55**, 1427–1435.

Fried, D. L.: 1966, 'Optical resolution through a randomly inhomogeneous medium for very long and very short exposures', *J. Opt. Soc. Am.* **56**, 1372–1379.

Glindemann, A.: 1997a, *Beating the Seeing Limit – Adaptive Optics on Large Telescopes*, Habilitationsschrift, Universität Heidelberg.

Glindemann, A.: 1997b, 'Relevant parameters for tip-tilt systems on large telescopes', *Publ. Astron. Soc. Pac.* **109**, 682–687.

Glindemann, A. and Berkefeld, T.: 1996, 'A New Method for Separating Atmospheric Layers using a Shack-Hartmann Curvature Sensor', in *Adaptive Optics, Vol. 13, 1996*, OSA Technical Digest Series. Washington DC, pp. 153–155.

Glindemann, A. and Rees, N. P.: 1993, 'UKIRT 5-Axis Tip-Tilt Secondary – Wavefront Sensor Simulations', in F. Merkle (ed.), *ICO-16 Satellite Conference on Active and Adaptive Optics*, Garching, Germany, pp. 273–278.

Glindemann, A. and Rees, N. P.: 1994, 'Photon Counting versus CCD Sensors for Wavefront Sensing – Performance Comparison in the Presence of Noise', in P. S. Idell (ed.), *Advanced Technology Optical Telescopes V*, Proc. SPIE 2199, pp. 824–834.

Goodman, J. W.: 1968, *Introduction to Fourier Optics*, McGraw-Hill, San Francisco.

Graves, J. E., Northcott, M. Roddier, F., Roddier, C. and Close, L.: 1998, 'First Light for Hokupa'a –

36 Element Curvature AO System at UH', in *Adaptive Optical Systems Technologies*, Proc. SPIE 3353, pp. 34–43.

Greenwood, D. P.: 1977, 'Bandwidth specification for adaptive optics systems', *J. Opt. Soc. Am.* **67**, 390–393.

Greenwood, D. P. and Fried, D. L.: 1976, 'Power spectra requirements for wave-front-compensative systems', *J. Opt. Soc. Am.* **66**, 193–206.

Haniff, C. A., Baldwin, J. E., Warner, P. J. and Scott, T. R.: 1994, 'Atmospheric Phase Fluctuation Measurement: Interferometric Results from the WHT and COAST Telescopes', in J. Breckinridge (ed.), *Amplitude and Spatial Interferometry II*, Proc. SPIE 2200, pp. 407–417.

Hardy, J. W., Lefebvre, J. E. and Koliopoulos, C. L.: 1977, 'Real-Time Atmospheric Compensation', *J. Opt. Soc. Am.* **67**, 360–369.

Hill, J. M.: 1996, 'The Large Binocular Telescope Project', in A. Ardeberg (ed.), *Optical Telescopes of Today and Tomorrow*, Proc. SPIE 2871, pp. 57–68.

Hufnagel, R. E.: 1974, 'Variations of Atmospheric Turbulence', in *Digest of Technical Papers, Topical Meeting on Optical Propagation through Turbulence*, Optical Society of America, Washington, D.C., pp. WAI/1-WAI/4.

Ishimura, A.: 1978, *Wave Propagation and Scattering in Random Media*, Academic, New York.

Johnston, D. C. and Welsh, B. M.: 1994, 'Analysis of multiconjugate adaptive optics', *J. Opt. Soc. Am.* **A11**, 394–408.

Kasper, M., Looze, D., Hippler, S. and Glindemann, A.: 1999, 'Choosing efficient basis sets for modal wavefront reconstruction with Shack-Hartmann sensors', in preparation.

Kasper, M. et al.: 2000, 'ALFA: Adaptive optics for the Calar Alto Observatory', *Experimental Astronomy* **10**(1), 49–73 (this issue).

Klückers, V. A., Wooder, N. J., Adcock, M. A., Nicholls, T. W. and Dainty, J. C.: 1998, 'Profiling of atmospheric turbulenee strength and velocity using a generalised SCIDAR technique', *Astronomy and Astrophysics Supplement* **130**, 141–155.

Kolmogorov, A. N.: 1961, 'The Local Structure of Turbulence in Incompressible Viscous Fluids for Very Large Reynolds' Numbers', in S. K. Friedlander and L. Topper (eds.), *Turbulence, Classical Papers on Statistical Theory*, pp. 151–155.

Lane, R. G. and Tallon, M.: 1992, 'Wave-front reconstruction using a Shack-Hartmann sensor', *Appl. Opt.* **31**, 6902–6908.

Law, N. F. and Lane, R. G.: 1996, 'Wavefront estimation at low light levels', *Opt. Commun.* **126**, 19–24.

Love, G., Andrews, N., Birch, P., Buscher, D., Doel, P., Dunlop, C., Major, J., Myers, R., Purvis, A., Sharples, R., Vick, A., Zadrozny, A., Restaino, S. R. and Glindemann, A.: 1995, 'Binary adaptive optics: atmospheric wave-front correction with a half-wave phase shifter', *nAppl. Opt.* **34**, 6058–6066.

Marathay, A. S.: 1982, *Elements of optical coherence theory*, J. Wiley & Sons, New York.

Martin, H. M.: 1987, 'Image motion as a measure of seeing quality', *Publ. Astron. Soc. Pac.* **99**, 1360–1370.

Melsa, J. L. and Cohn, D. L.: 1978, *Decision and Estimation Theory*, McGraw-Hill, New York.

Merkle, F., Kern, P., Léna, P., Rigaut, F., Fontanella, J. C., Rousset, G., Boyer, C., Gaffard, J. P. and Jagourel, P.: 1989, 'Successful tests of adaptive optics', *ESO Messenger* **58**, 1–4.

Noll, R. J.: 1976, 'Zernike polynomials and atmospheric turbulence', *J. Opt. Soc. Am.* **66**, 207–211.

Obukhov, A. M.: 1949, *Izv. Akad. Nauk S. S. S. R., Ser Geograf. Geofiz.* **13**, 58.

Primot, J., Rousset, G. and Fontanella, J. C.: 1990, 'Deconvolution from wave-front sensing: A new technique for compensating turbulence-degraded images', *J. Opt. Soc. Am.* **A7**, 1598–1608.

Ribak, E. N.: 1994, 'Deformable Mirros', in D. M. Alloin and J. M. Mariotti (eds.), *Adaptive Optics for Astronomy*, pp. 149–162.

Ribak, E. N., Gershnik, E. and Cheselka, M.: 1996, 'Stellar Scintillations as a remote atmospheric wave-front sensor', *Opt. Lett.* **21**, 435–437.

Rigaut, F.: 1994, 'Astronomical Reference Sources', in D. M. Alloin and J. M. Mariotti (eds.), *Adaptive Optics for Astronomy*, pp. 163–183.

Rigaut, F.: 1997, 'Performance of the Canada-France-Hawaii Telescope Adaptive Optics Bonnette', *Astronomy and Astrophysics*, in preparation.

Rigaut, F. and Gendron, E.: 1992, 'Laser guide star in adaptive optics: The tilt determination problem', *Astronomy and Astrophysics* **261**, 677–684.

Roddier, F.: 1981, 'The Effects of Atmospheric Turbulence in Optical Astronomy', in E. Wolf (ed.), *Progress in Optics XIX*, Amsterdam, North-Holland, pp. 281–376.

Roddier, F.: 1988, 'Curvature sensing and compensation: A new concept in adaptive optics', *Appl. Opt.* **27**, 1223–1225.

Roddier, F.: 1990a, 'Wavefront sensing and the irradiance transport equation', *Appl. Opt.* **29**, 1402–1403.

Roddier, F.: 1990b, 'Atmospheric wavefront simulation using Zemike polynomials', *Opt. Eng.* **29**, 1174–1180.

Roddier, F: 1995, 'Error propagation in a closed-loop adaptive optics system: A comparison between Shack-Hartmann and curvature wave-front sensors', *Opt. Commun.* **113**, 357–359.

Roddier, F. (ed.): 1999, *Adaptive Optics in Astronomy*, Cambridge University Press.

Roddier, F., Gilli, J. M. and Lund, G.: 1982, 'On the origin of speckle boiling and its effects in stellar speckle interferometry', *J. Optics (Paris)* **13**, 263–271.

Roddier, F., Northcott, M. and Graves, J. E.: 1991, 'A simple low-order adaptive optics system for near-infrared applications', *Publ. Astron. Soc. Pac.* **103**, 131–149.

Roddier, F., Northcott, M. J., Graves, J. E., McKenna, D. L. and Roddier, D.: 1993, 'One-dimensional spectra of turbulence-induced Zemike aberrations: Time-delay and isoplanicity error in partial adaptive compensation', *J. Opt. Soc. Am.* **A10**, 957–965.

Roggemann, M. C. and Welsh, B. M.: 1996, *Imaging through the Atmosphere*, CRC, Boca Raton.

Rousset, G.: 1994, 'Wavefront Sensing', in D. M. Alloin and J. M. Mariotti (eds.), *Adaptive Optics for Astronomy*, pp. 115–137.

Salinari, P., Vecchio, C. D. and Biliotti, V.: 1993, 'A Study of an Adaptive Secondary Mirror', in: F. Merkle (ed.), *ICO-16 Satellite Conference of Active and Adaptive Opties*, Garching, Germany, pp. 247–253.

Sallberg, S. A., Welsh, B. M. and Roggemann, M. C.: 1997, 'Maximum a posteriori estimation of wave-front slopes using a Shack-Hartmann wave-front sensor', *J. Opt. Soc. Am.* **A6**, 1347–1354.

Tatarski, V. I.: 1961, *Wave Propagation in a Turbulent Medium*, McGraw-Hill, New York.

Tatarski, V. I. and Zavorotny, V. U.: 1993, 'Atmospheric turbulence and the resolution limits of large ground-based telescopes: Comment', *J. Opt. Soc. Am.* **A10**, 2410–2417.

Tyler, G. A.: 1994, 'Bandwidth considerations for tracking through turbulence', *J. Opt. Soc. Am.* **A11**, 358–367.

Tyson, R. K.: 1998, *Principles of Adaptive Opties*, 2nd ed., Academic Press, San Diego.

Valley, G. C.: 1980, 'Isoplanatic degradation of tilt correction and short-term imaging systems', *Appl. Opt.* **19**, 574–577.

Vdovin, G. and Sarro, P. M.: 1995, 'Flexible mirror micromachined in silicon', *Appl. Opt.* **34**, 2968–2972.

Vernin, J. and Roddier, F.: 1973, 'Experimental determination of two-dimensional spatiotemporal power spectra of stellar light scintillation. Evidence for a multilayer structure of the air turbulence in the upper troposphere', *J. Opt. Soc. Am.* **63**, 270–273.

Wallner, E. P.: 1983, 'Optimal wave-front correction using slope measurements', *J. Opt. Soc. Am.* **73**, 1771–1776.

Weast, R. C. and Astle, M. J. (eds.): 1981, *CRC Handbook of Chemistry and Physics*, CRC, Boca Raton.

Zemike, F.: 1934, *Physica* **1**, 689.